The Astrophysical Journal, 939:8 (18pp), 2022 November 1 https://doi.org/10.3847/1538-4357/ac8c36

Lanthanide Features in Near-infrared Spectra of Kilonovae

Nanae Domoto[1], Masaomi Tanaka[1,2], Daiji Kato[3,4], Kyohei Kawaguchi[5,6], Kenta Hotokezaka[7,8], and Shinya Wanajo[9,10]

[1] Astronomical Institute, Tohoku University, Aoba, Sendai 980-8578, Japan; n.domoto@astr.tohoku.ac.jp
[2] Division for the Establishment of Frontier Sciences, Organization for Advanced Studies, Tohoku University, Sendai 980-8577, Japan
[3] National Institute for Fusion Science, 322-6 Oroshi-cho, Toki 509-5292, Japan
[4] Interdisciplinary Graduate School of Engineering Sciences, Kyushu University, Kasuga, Fukuoka 816-8580, Japan
[5] Institute for Cosmic Ray Research, The University of Tokyo, 5-1-5 Kashiwanoha, Kashiwa, Chiba 277-8582, Japan
[6] Center for Gravitational Physics, Yukawa Institute for Theoretical Physics, Kyoto University, Kyoto 606-8502, Japan
[7] Research Center for the Early Universe, Graduate School of Science, University of Tokyo, Bunkyo, Tokyo 113-0033, Japan
[8] Kavli IPMU (WPI), UTIAS, The University of Tokyo, Kashiwa, Chiba 277-8583, Japan
[9] Max-Planck-Institut für Gravitationsphysik (Albert-Einstein-Institut), Am Mühlenberg 1, D-14476 Potsdam-Golm, Germany
[10] Interdisciplinary Theoretical and Mathematical Sciences Program (iTHEMS), RIKEN, Wako, Saitama 351-0198, Japan
Received 2022 June 8; revised 2022 August 14; accepted 2022 August 22; published 2022 October 26

Abstract

The observations of GW170817/AT2017gfo have provided us with evidence that binary neutron star mergers are sites of *r*-process nucleosynthesis. However, the observed signatures in the spectra of GW170817/AT2017gfo have not been fully decoded, especially in the near-infrared (NIR) wavelengths. In this paper, we investigate the kilonova spectra over the entire wavelength range with the aim of elemental identification. We systematically calculate the strength of bound–bound transitions by constructing a hybrid line list that is accurate for important strong transitions and complete for weak transitions. We find that the elements on the left side of the periodic table, such as Ca, Sr, Y, Zr, Ba, La, and Ce, tend to produce prominent absorption lines in the spectra. This is because such elements have a small number of valence electrons and low-lying energy levels, resulting in strong transitions. By performing self-consistent radiative transfer simulations for the entire ejecta, we find that La III and Ce III appear in the NIR spectra, which can explain the absorption features at $\lambda \sim 12000$–14000 Å in the spectra of GW170817/AT2017gfo. The mass fractions of La and Ce are estimated to be $>2 \times 10^{-6}$ and $\sim(1\text{–}100) \times 10^{-5}$, respectively. An actinide element Th can also be a source of absorption as the atomic structure is analogous to that of Ce. However, we show that Th III features are less prominent in the spectra because of the denser energy levels of actinides compared to those of lanthanides.

Unified Astronomy Thesaurus concepts: R-process (1324); Neutron stars (1108); Radiative transfer simulations (1967); Atomic physics (2063)

1. Introduction

Binary neutron star (NS) mergers are promising sites of rapid neutron capture nucleosynthesis (*r*-process, e.g., Lattimer & Schramm 1974; Eichler et al. 1989; Meyer 1989; Freiburghaus et al. 1999; Goriely et al. 2011; Korobkin et al. 2012; Wanajo et al. 2014). Radioactive decay of freshly synthesized nuclei in the ejected neutron-rich material powers electromagnetic emission called a kilonova (Li & Paczyński 1998; Metzger et al. 2010; Roberts et al. 2011). In 2017, together with the detection of gravitational waves (GW) from an NS merger (GW170817, Abbott et al. 2017a), an electromagnetic counterpart was identified (AT2017gfo, Abbott et al. 2017b). The observed properties of AT2017gfo in ultraviolet, optical, and near-infrared (NIR) wavelengths are consistent with the theoretical expectation of a kilonova (e.g., Arcavi et al. 2017; Coulter et al. 2017; Evans et al. 2017; Pian et al. 2017; Smartt et al. 2017; Utsumi et al. 2017; Valenti et al. 2017). The electromagnetic counterpart has provided us with evidence that NS mergers are sites of *r*-process nucleosynthesis (e.g., Kasen et al. 2017; Perego et al. 2017; Shibata et al. 2017; Tanaka et al. 2017; Kawaguchi et al. 2018; Rosswog et al. 2018).

It is important to reveal the abundance pattern in NS merger ejecta. However, the elemental abundances synthesized in GW170817 are not yet clear. One of the direct ways of finding the synthesized elements is the identification of absorption lines in photospheric spectra. Watson et al. (2019) analyzed the observed spectra of GW170817/AT2017gfo a few days after the merger. Based on spectral calculations above the photosphere, they found that the absorption features around $\lambda \sim 8000$ Å could be explained by the Sr II lines (see also Gillanders et al. 2022). Domoto et al. (2021) carried out self-consistent radiative transfer simulations of the entire ejecta, and also showed that Sr II produces strong absorption lines. Perego et al. (2022) suggested the presence of He as an alternative explanation of the features around $\lambda \sim 8000$ Å, but ultimately concluded that this was unlikely. While the observed spectra exhibit several features, especially at NIR wavelengths, no other element has yet been identified (see Gillanders et al. 2021 for a search of Pt and Au).

Synthesized elements can also be identified in the spectra during the nebula phase because of the appearance of emission lines. In GW170817, the Spitzer space telescope detected the late-time nebular emission at 4.5 μm and put an upper limit at 3.6 μm, suggesting distinctive spectral features (Villar et al. 2018; Kasliwal et al. 2022). Recently, Hotokezaka et al. (2021) and Pognan et al. (2022a, 2022b) have initiated work on the nebula phase of a kilonova. Although conclusive identification

of elements has not been made with the spectra, it is suggested that the IR nebula emission in GW170817 can be explained mainly by the lines of Se ($Z = 34$) or W ($Z = 74$) (Hotokezaka et al. 2022).

One of the issues facing the study of kilonova spectra is a lack of atomic data for heavy elements. To extract elemental information from the spectra, spectroscopically accurate atomic data are needed. However, since such atomic data are not complete, especially for heavy elements at NIR wavelengths, we have been able to investigate lines only at the optical wavelengths, $\lambda \lesssim 10000$ Å (Watson et al. 2019; Domoto et al. 2021). Although the incompleteness of the data can be mitigated by theoretical calculations (e.g., Kasen et al. 2013; Tanaka et al. 2018, 2020; Banerjee et al. 2020; Fontes et al. 2020; Pognan et al. 2022b), such theoretical data require calibration with experimental data for quantitative discussion on spectral features, due to the low accuracy in wavelengths (Gillanders et al. 2021).

In this paper, we propose a new scheme to investigate the spectral features over the whole wavelength range with the aim of elemental identification in kilonova photospheric spectra. In Section 2, we systematically calculate the strength of bound–bound transitions by means of a simple one-zone model using theoretical atomic data. By combining atomic data based on theoretical calculations and experiments, we construct a new hybrid line list that is accurate for important strong transitions and complete for weak transitions. Then, in Section 3, we perform radiative transfer simulations of NS merger ejecta with the new line list. In Section 4, we discuss the estimated lanthanide abundances in GW170817/AT2017gfo and the possibilities of identifying actinide elements. Finally, we give our conclusions in Section 5.

2. Line List

To evaluate the strength of bound–bound transitions in NS merger ejecta, we essentially need atomic data. In this paper, a data set of transition wavelength, energy level of transition, and transition probability is referred to as a line list.

For theoretical calculations of kilonova light curves, atomic data obtained from theoretical calculations have been often used (e.g., Kasen et al. 2013; Tanaka et al. 2018, 2020; Banerjee et al. 2020; Fontes et al. 2020). This is useful in terms of completeness of the transition lines, because the opacity of ejecta should be correctly evaluated for light curve calculations. However, while such theoretical data give a reasonable estimate for the total opacity, they are not necessarily accurate in transition wavelengths, and thus, not suitable for element identification.

Domoto et al. (2021) used the latest line list constructed from the Vienna Atomic Line Database (VALD; Piskunov et al. 1995; Kupka et al. 1999; Ryabchikova et al. 2015) to focus on the imprint of elemental abundances in kilonova spectra. This database is suitable for identifying lines because the atomic data are calibrated with experiments and semiempirical calculations. Since most spectroscopic experiments have been conducted in the optical range, there is enough data to investigate spectral features at optical wavelengths. However, such an experimental line list is not necessarily complete in the NIR region.

Here, we propose a new scheme to take advantage of both line lists. By using a complete line list constructed from theoretical calculations, we first identify which elements can show strong transitions under the physical conditions of NS merger ejecta. Then, we calibrate the theoretical energy levels with experimental data and construct an accurate line list for the selected ions with strong transitions. In this way, we construct a hybrid line list that is complete for weak transitions and accurate for strong transitions, which are important for element identification.

2.1. Candidate Species

To investigate which elements can become absorption sources in kilonova photospheric spectra, we systematically calculate the strength of bound–bound transitions for a given density, temperature, and element abundances. The strength of a line is approximated by the Sobolev optical depth (Sobolev 1960) for each bound–bound transition,

$$\begin{aligned}\tau_l &= \frac{\pi e^2}{m_e c} n_{i,j,k} t \lambda_l f_l \\ &= \frac{\pi e^2}{m_e c} n_{i,j} t \lambda_l f_l \frac{g_k}{g_0} e^{-\frac{E_k}{kT}}, \end{aligned} \quad (1)$$

in homologously expanding ejecta. The Sobolev approximation is valid for matter with a high expansion velocity and a large radial velocity gradient. Here, $n_{i,j,k}$ is the number density of ions at the lower level of a transition (i-th element, j-th ionization stage, and k-th excited state), f_l and λ_l are the oscillator strength and the transition wavelength, g_0 is the statistical weight at the ground state, and g_k and E_k are the statistical weight and the lower energy level of a bound–bound transition, respectively. As in previous work on kilonovae (e.g., Barnes & Kasen 2013; Tanaka & Hotokezaka 2013), we assume local thermodynamic equilibrium (LTE); we solve the Saha equation to obtain ionization states, and assume Boltzmann distribution for the population of excited levels, which appears in Equation (1) (see Pognan et al. 2022a for non-LTE effects).

For the abundances in the ejected matter from an NS merger, we use the same model as in Domoto et al. (2021) based on a multicomponent free-expansion (mFE) model of Wanajo (2018). Here, we use the Light (L) model as our fiducial model (the left panel of Figure 1), which exhibits a similar abundance pattern to that of metal-poor stars with weak r-process signature (e.g., HD 122563, Honda et al. 2006, the right panel of Figure 1). This is motivated by the fact that the blue emission of GW170817/AT2017gfo a few days after the merger is suggested to have stemmed from the ejecta component dominated by relatively light r-process elements (e.g., Arcavi et al. 2017; Nicholl et al. 2017; Tanaka et al. 2017, 2018). Although the model includes the abundances with the atomic number of $Z = 1$–110, we use only the abundances at $t = 1.5$ days with $Z = 20$–100 in our calculations as shown in the right panel of Figure 1. The mass fractions of elements relevant to this study are summarized in Table 1. Note that the calculated abundances, which are recomputed with an updated nucleosynthesis code (Fujibayashi et al. 2020, 2022), slightly differ (within a factor of 2 at 1.5 days) from those presented in Domoto et al. (2021). We have confirmed that our new nucleosynthetic abundances give almost the same results as those in Domoto et al. (2021).

For the atomic data, we use a theoretical line list from Tanaka et al. (2020). This line list was constructed for the

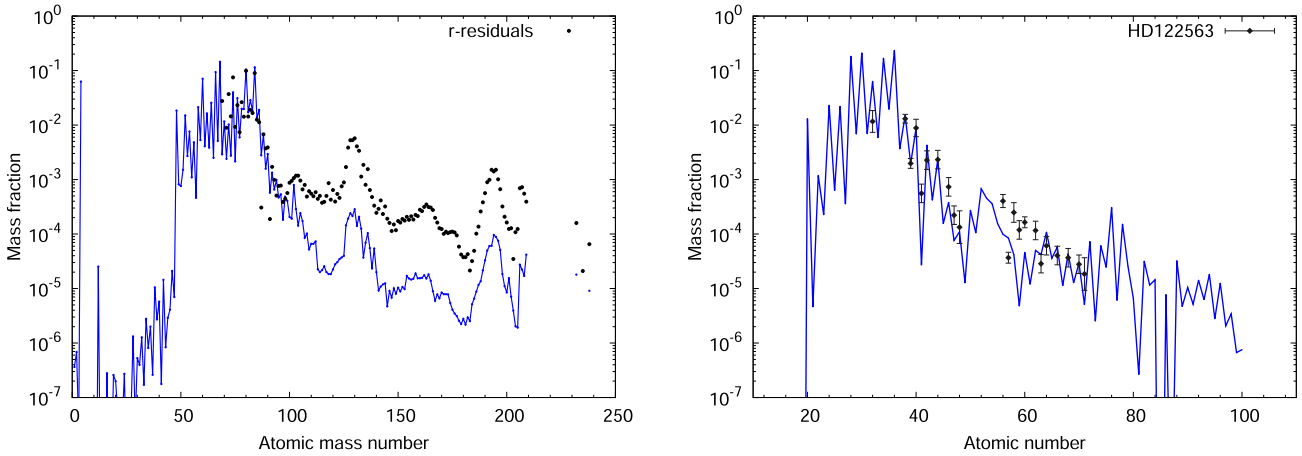

Figure 1. Left: final abundances of our L model as a function of mass number. Black circles show the *r*-process residual pattern (Prantzos et al. 2020), which are scaled to match those for the L model at $A = 88$. Right: abundances at $t = 1.5$ days as a function of atomic number. Abundances of an *r*-process-deficient star HD 122563 (diamonds, Honda et al. 2006; Ge from Cowan et al. 2005; Cd and Lu from Roederer et al. 2012) are also shown for comparison, and are scaled to match those for the L model at $Z = 40$.

Table 1
Mass Fractions of Selected Elements in the L Model

X(Ca)	X(Sr)	X(Y)	X(Zr)	X(Ba)	X(La)	X(Ce)	X(Th)	X(La+Ac)[a]
1.8×10^{-2}	6.8×10^{-3}	1.6×10^{-3}	6.4×10^{-2}	1.5×10^{-4}	5.4×10^{-5}	3.1×10^{-5}	1.8×10^{-5}	4.9×10^{-4}
1.3×10^{-2}	1.5×10^{-2}	2.0×10^{-3}	8.8×10^{-3}	9.9×10^{-5}	8.5×10^{-5}	4.2×10^{-5}	1.0×10^{-5}	6.7×10^{-4}

Notes. The top and bottom rows show the final abundances and those at $t = 1.5$ days, respectively.
[a] Sum of mass fractions for lanthanides ($Z = 57$–71) and actinides ($Z = 89$–100).

elements with $Z = 30$–88 from neutral atoms up to triply ionized ions by systematic atomic structure calculations using the HULLAC code (Bar-Shalom et al. 2001). Since transition data of this line list are not necessarily accurate in terms of wavelengths, we here only study the species of ions to produce strong transitions.

Note that the theoretical line list does not include the data for actinides ($Z = 89$–100) due to the difficulty of atomic structure calculations (Tanaka et al. 2020). While actinides just work as zero-opacity sources without atomic data, we keep these elements in the list to discuss the spectral features of actinides in Section 4.2.

The strength of bound–bound transitions at $t = 1.5$ and 3.5 days for the L model is shown in the top panels of Figure 2. We evaluate the Sobolev optical depth for the density of $\rho = 10^{-14}$ g cm^{-3} and the temperature of $T = 5000$ K at $t = 1.5$ days, and $\rho = 10^{-15}$ g cm^{-3} and $T = 3000$ K at $t = 3.5$ days. These are typical values in the line-forming region when we adopt the abundance distribution of the L model (see Figure 6).

We find that, among all the elements, Y II, Zr II, La III, and Ce III lines are as strong as the Sr II triplet lines under the condition at $t = 1.5$ days. On the other hand, under the condition at $t = 3.5$ days, Y I, Zr I, and Ba II lines appear instead of Zr II, La III, and Ce III lines. Although the individual lines of Zr I are not by far the strongest, they can be important absorption sources due to the fact that the multiple lines show comparable strength at a certain wavelength range.

The behavior of the strength of the lines can be understood as the dependence of the Sobolev optical depths on temperature and density (Figure 4 of Domoto et al. 2021). When the density is $\rho = 10^{-14}$–10^{-15} g cm^{-3}, the strength of Sr II triplet lines does not show a large difference between $T = 3000$ and 5000 K. This is determined by the combination of the ionization fraction and the population of the levels at these temperatures. While the lines of singly ionized Sr ($Z = 38$) are not largely affected in this temperature range, the lines of neutral Y ($Z = 39$) and Zr ($Z = 40$) appear at $T = 3000$ K. This is due to the slightly higher ionization potentials of Y and Zr. On the other hand, the strength of Ce III lines largely changes in this temperature range reflecting the ionization fraction. Most Ce atoms are singly ionized at $T = 3000$ K, and thus, the lines of Ce III become weaker at a lower temperature. The behavior of Ba II ($Z = 56$) and La III ($Z = 57$) lines can be explained in a similar way to that of Ce III ($Z = 58$).

2.2. Atomic Properties

Although our line list includes all elements with $Z = 30$–88, our results indicate that only a few elements, such as Sr, Y, Zr, Ba, La, and Ce can become strong absorption sources in the spectra. The reason can be interpreted by the atomic properties of these elements. From Equation (1), the necessary conditions for a given line to become strong are that (1) the transition probability ($g_k f_l$) is high and (2) the lower energy level of the transition (E_k) is low (i.e., the level population is high).

The left panel of Figure 3 shows the mean values of log gf for all the lines of singly ionized ions as a function of atomic number. The mean gf-values show the pattern according to the orbital angular momentum l of the valence shell. This is more understandable when we use the complexity of a given ion, defined as (Kasen et al. 2013):

$$C = \Pi_m \frac{g_m!}{n_m!(g_m - n_m)!}, \quad (2)$$

where $g = 2(2l + 1)$ is the number of magnetic sublevels in the subshell with orbital angular momentum l, and n_m is the

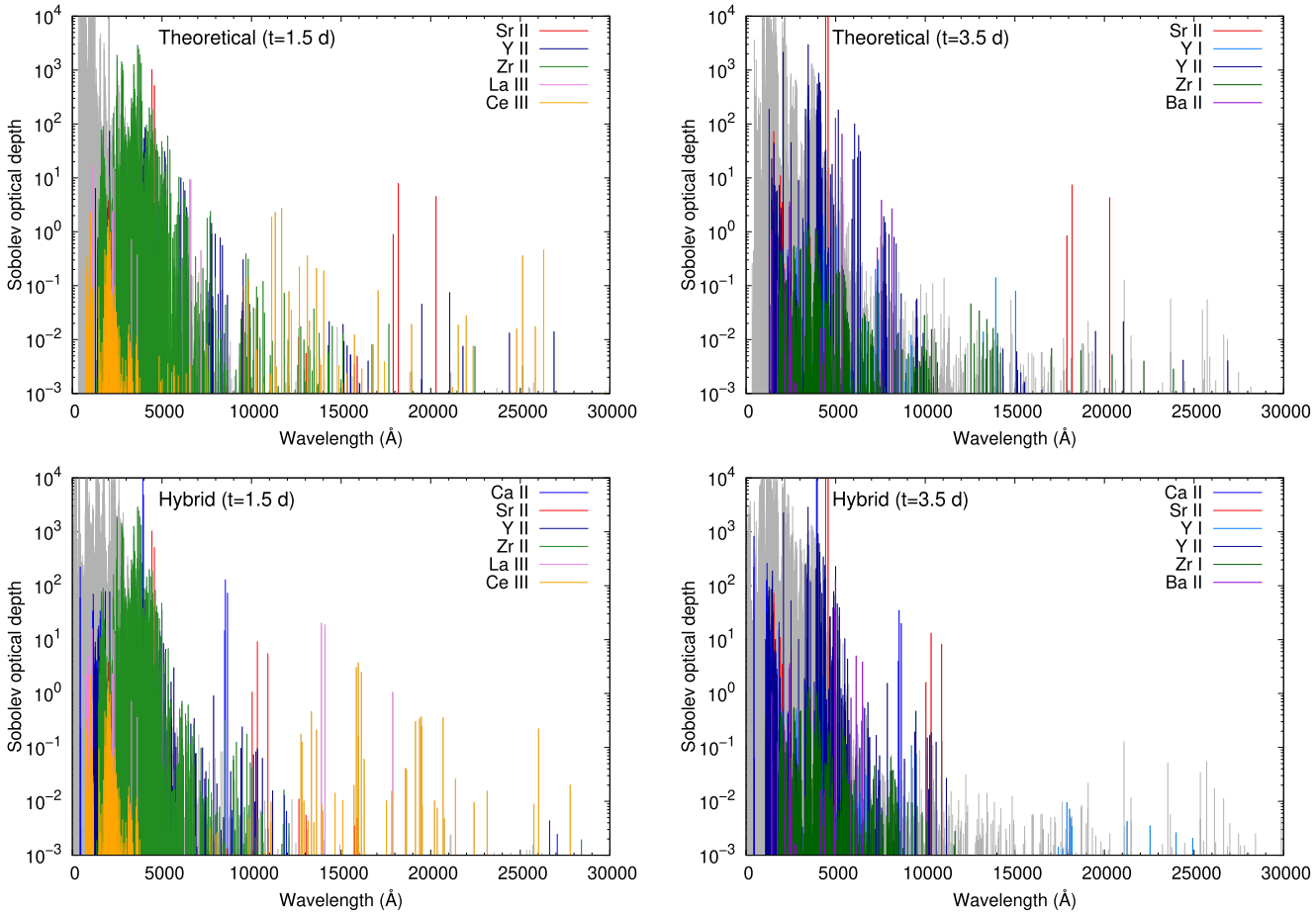

Figure 2. Sobolev optical depth of bound–bound transitions for the L model calculated with the theoretical line list (Tanaka et al. 2020 $Z = 30$–88, top) and those calculated with the hybrid line list ($Z = 20$–88, bottom, Section 2.3). The ions with large contributions are shown with colors. The left panels show the results with the density of $\rho = 10^{-14}$ g cm^{-3} and the temperature of $T = 5000$ K at $t = 1.5$ days, while the right panels show those with $\rho = 10^{-15}$ g cm^{-3} and $T = 3000$ K at $t = 3.5$ days.

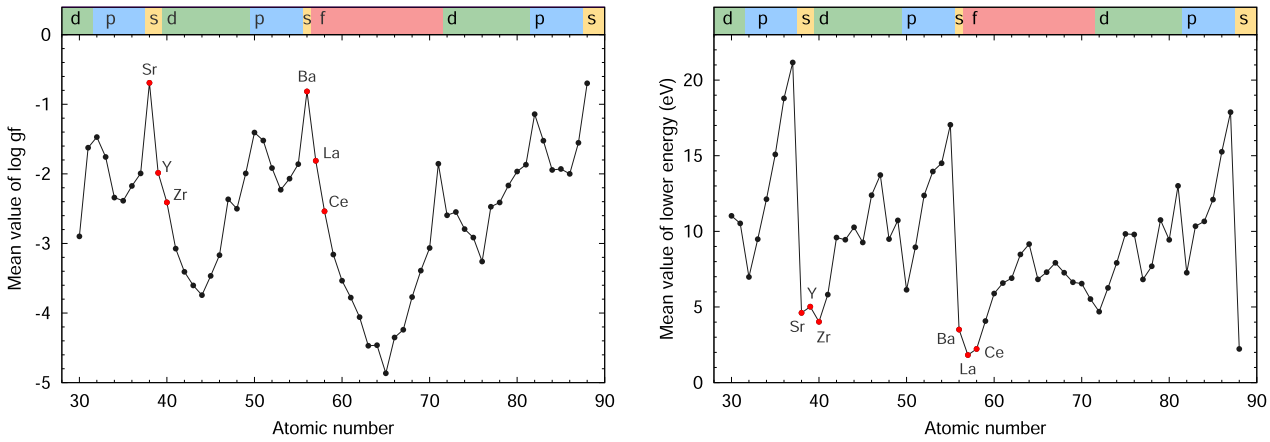

Figure 3. Mean values of log gf (left) and of lower energies of transitions (right) for all the lines of singly ionized ions as a function of atomic number. Colors at the top show the valence shells with the orbital angular momenta l for singly ionized ions. Red circles indicate the elements that produce strong transitions in our analysis (see the text).

number of electrons in the nl-orbital labeled m. The complexity indicates how dense the energy levels are packed, and takes the maximal value when filling half the closed shell (Figure 1 of Kasen et al. 2013). Figure 4 shows the number of lines and the mean value of log gf for singly ionized ions as a function of complexity. We find that the complexity shows a positive correlation with the number of lines. It is natural because the number of transition combinations increases for larger complexity, i.e., denser energy levels. We also find that the complexity shows a negative correlation with the mean gf-value. This can be understood by the sum rule of oscillator strength; when the ion has a larger number of transitions, the oscillator strength of each line tends to be smaller. Other ionization states are not presented in Figure 4, but show similar

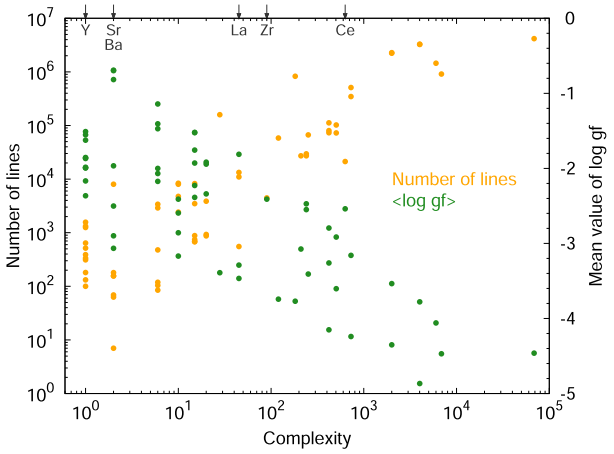

Figure 4. The number of lines (orange) and mean value of log *gf* (green) for singly ionized ions as a function of complexity.

trends. Therefore, the ions with relatively low complexity are likely to have transitions with relatively high *gf*-values.

The right panel of Figure 3 shows the mean values of the lower energy levels of transitions for all the lines of singly ionized ions as a function of atomic number. The mean lower energy level of transitions tends to be pushed up toward higher energy as atomic number increases in an electron shell series. Other ionization states also show similar behavior. As spin–orbit interaction energy strongly depends on atomic number, energy-level spacing at a certain shell increases with atomic number. Also, electron orbital radii become smaller as atomic number increases, so that electron–electron interaction energies become higher for larger atomic numbers. As a result, the distribution of energy levels becomes wider for larger atomic numbers at a given shell (Tanaka et al. 2020). Therefore, the ions with smaller atomic numbers in a certain period on the periodic table tend to have transitions from low-lying energy levels.

Consequently, it is natural that Sr, Y, Zr, Ba, La, and Ce show strong lines. According to the two properties mentioned above, the ions on the left side of the periodic table are anticipated to show strong lines. In fact, all of the elements showing strong lines belong to groups 2 to 4 on the periodic table; in other words, they have a relatively small number of valence electrons (low complexity) and relatively low-lying energy levels.

Among these ions, La III and Ce III show strong lines at the NIR wavelengths (Figure 2). This can be understood from the properties of lanthanide elements. While lanthanide elements are characterized by having the 4*f*-electrons, the configurations of low-lying energy levels for lanthanides also involve the outer 5*d* and 6*s* shells. This means that the energy scales of 4*f*, 5*d*, and 6*s* orbitals for lanthanides are similar; in other words, the energy differences between these orbitals are small. In fact, the strong transitions of La III and Ce III at the NIR wavelengths involve an electron jump between 4*f* and 5*d* orbitals (see Tables 3 and 4). Thus, it is natural that La III and Ce III lines tend to appear in the NIR region.

2.3. Construction of Hybrid Line List

We find that Y, Zr, Ba, La, and Ce, as well as Sr, can show strong lines under the physical conditions of NS merger ejecta. To enable us to inspect absorption lines produced by these elements in kilonova photospheric spectra, we calibrate the energy levels and resulting transition wavelengths of theoretical atomic data with experimental data. The details for calibration procedures are given in Appendix A.

Table 2
Summary of the Hybrid Line List

	Element[a]	Ion	Reference	
			Levels	Transitions
Baseline	$Z = 20$–29	I–IV	1	
	$Z = 30$–88	I–IV	2	
	$Z = 89$–100		no lines	
Calibrated ions	Sr ($Z = 38$)	II	3	1
	Y ($Z = 39$)	I, II	3	1
	Zr ($Z = 40$)	I, II	3	4
	Ba ($Z = 56$)	II	3	1
	La ($Z = 57$)	III	3	2
	Ce ($Z = 58$)	III	3	2
Section 4.2	Th ($Z = 90$)	III	3	1 (optical) 3, 5 (NIR)[b]

Notes.
[a] Elements of $Z = 20$–100 are used for all the calculations in this paper.
[b] Relative intensities are used to estimate the transition probabilities (see Section 4.2).
References: (1) VALD (Piskunov et al. 1995; Kupka et al. 1999; Ryabchikova et al. 2015); (2) Tanaka et al. (2020); (3) NIST Atomic Spectral Database (Kramida et al. 2021); (4) Kurucz's atomic data (Kurucz 2018); (5) Engleman (2003).

To use the calibrated lines in radiative transfer simulations (Section 3), we need their transition probabilities. After calibrating the energy levels and wavelengths, the transition probabilities of the calibrated lines are taken from the VALD database (Piskunov et al. 1995; Kupka et al. 1999; Ryabchikova et al. 2015) or Kurucz's atomic data (Kurucz 2018) if the lines are listed, otherwise theoretical values from Tanaka et al. (2020) are adopted. The general validity of the theoretical transition probabilities is discussed in Appendix A. The transitions with the theoretical transition probabilities are summarized in Tables 3–4 (Appendix A).

Finally, we construct a hybrid line list by combining the VALD database for $Z = 20$–29 and the results of atomic calculations from Tanaka et al. (2020) for $Z = 30$–88. Among the data of $Z = 30$–88, strong transitions of Sr II, Y I, Y II, Zr I, Zr II, Ba II, La III, and Ce III are replaced with those calibrated with experimental data. The information for the hybrid line list is summarized in Table 2. The bottom panels of Figure 2 show the strength of bound–bound transitions at $t = 1.5$ and 3.5 days calculated with the new hybrid line list. In these panels, the wavelengths of strong transitions are accurate as they are calibrated with experimental data. We find that La III and Ce III lines become strong absorption sources at the NIR wavelengths at $t = 1.5$ days. For Y I, Y II, Zr I, Zr II, and Ba II, most of the wavelengths of relatively strong lines are found to be placed in the optical region ($\lambda < 10000$ Å). Thus, their lines are unlikely to produce absorption features in the NIR region, although they may be important absorption sources at the optical wavelengths (see Section 3).

We adopt the theoretical transition probabilities when they are not available in the VALD database or Kurucz's line list.

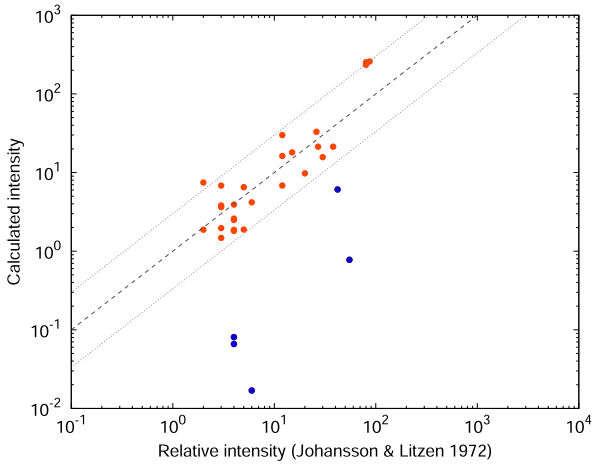

Figure 5. Comparison of intensities for NIR Ce III lines between those calculated with theoretical *gf*-values and those measured by experiments (Johansson & Litzén 1972). Gray dashed and dotted lines correspond to perfect agreement and deviations by a factor of 3, respectively. Blue circles indicate the lines whose theoretical *gf*-values are underestimated more than a factor of 3.

To validate the accuracy of theoretical *gf*-values for NIR lines, we use the relative intensities of Ce III lines. Johansson & Litzén (1972) measured the emission lines of Ce III at the NIR wavelengths in a laboratory and showed the relative intensities of measured lines. Assuming LTE for ionization and excitation, the intensity of an emission line can be calculated as

$$I = b\ g_u A\ e^{-\frac{E_u}{kT}} = b\frac{8\pi e^2}{m_e c \lambda_l^2} g_l f_l e^{-\frac{E_u}{kT}}, \quad (3)$$

where A, g_u, and E_u are Einstein's A coefficient, the statistical weight, and the energy level of the upper level for a transition, respectively, and b is a constant depending on the ion species. Since plasma in experiments is typically in LTE due to the high density of ions (Kielkopf 1971), we can use this formula to evaluate the *gf*-values of Ce III lines.

A comparison between the intensities of Ce III lines calculated with the theoretical transition probabilities and those measured by experiments (Johansson & Litzén 1972) is shown in Figure 5. We adopt the temperature of $T = 12000$ K, which is a typical plasma temperature in experiments (Kielkopf 1971). Here a normalization factor b is set so that the calculated values are close to the experimental values. We find that the calculated and experimentally measured intensities are in good agreement except for a few lines. Since in the situation we consider ($E_u \lesssim 2$ eV), the intensities are mainly determined by transition probabilities, the trend suggests that our theoretical *gf*-values of Ce III lines are reasonable. We note that, although the *gf*-values of a few lines should be higher than our estimates (blue circles in Figure 5), they are relatively weak and do not affect our conclusions. Nevertheless, to determine the exact values of transition probabilities for these lines, more experimental and observational calibrations are necessary for the NIR region.

3. Synthetic Spectra

3.1. Methods

In this section, we calculate realistic synthetic spectra of kilonovae by using the new hybrid line list. We use a wavelength-dependent radiative transfer simulation code (Tanaka & Hotokezaka 2013; Tanaka et al. 2014, 2017, 2018; Kawaguchi et al. 2018, 2020). The photon transfer is calculated by the Monte Carlo method. To compute the opacity for bound–bound transitions, we adopt the expansion opacity (Karp et al. 1977) and use the formula from Eastman & Pinto (1993):

$$\kappa_{\rm exp}(\lambda) = \frac{1}{ct\rho}\sum_l \frac{\lambda_l}{\Delta\lambda}(1 - e^{-\tau_l}), \quad (4)$$

where τ_l is the Sobolev optical depth (Equation (1)). In the equation, the summation is taken over all transitions within a wavelength bin $\Delta\lambda$ (see below). The Sobolev optical depth is evaluated by assuming LTE for ionization and excitation as in Section 2.1.

For the atomic data, we use the new hybrid line list constructed in Section 2.3. The hybrid line list still includes weak transitions whose wavelengths are not necessarily accurate. To avoid the substantial effects of these lines on spectra, we adopt a wide wavelength grid for the opacity calculation with the atomic data from theoretical calculations (i.e., lines for $Z = 30$–88). The wavelength grid is typically set to $\Delta\lambda = 10$ Å (Tanaka & Hotokezaka 2013), but here a 20 times wider grid is adopted for the theoretical line list. This smears out the individual effect of each line on the bound–bound opacity. We also performed the same opacity calculations with the typical fine wavelength grid, and confirmed that the resultant total opacity is almost unchanged. For the accurate transitions (i.e., lines for $Z = 20$–29 and calibrated lines), we adopt $\Delta\lambda = 10$ Å. By combining the opacity calculated with the theoretical atomic data and the strong transitions calculated with the accurate data, we are able to discuss whole spectral features, i.e., an overall shape, absorption lines, and their time evolution.

In the radiative transfer code, the temperature in each cell is determined by the photon flux (Lucy 2003; Tanaka & Hotokezaka 2013). The photon intensity is evaluated as

$$J_\nu d\nu = \frac{1}{4\pi\Delta t V}\sum_{d\nu} \epsilon\, ds, \quad (5)$$

where ϵ is the comoving-frame energy of a photon packet. The temperature is estimated by assuming that the wavelength-integrated intensity $\langle J\rangle = \int J_\nu d\nu$ follows the Stefan–Boltzmann law, i.e.,

$$\langle J\rangle = \frac{\sigma}{\pi} T_R^4. \quad (6)$$

The kinetic temperature of electrons T_e is assumed to be the same as the radiation temperature T_R, i.e., $T = T_e = T_R$ under LTE.

For the ejecta density structure, we assume a single power law ($\rho \propto r^{-3}$) for the velocity range of ejecta $v = 0.05$–$0.3c$ (e.g., Metzger et al. 2010). The total ejecta mass is set to be $M_{\rm ej} = 0.03\,M_\odot$, which is suggested to explain the observed luminosity of AT2017gfo (e.g., Tanaka et al. 2017; Kawaguchi et al. 2018). For the abundance distribution, we use the same model (L model) as described in Section 2.1. The heating rate of radioactive nuclei as a function of time is consistently computed for this model. The thermalization efficiency of γ-rays and radioactive particles follows the analytic formula

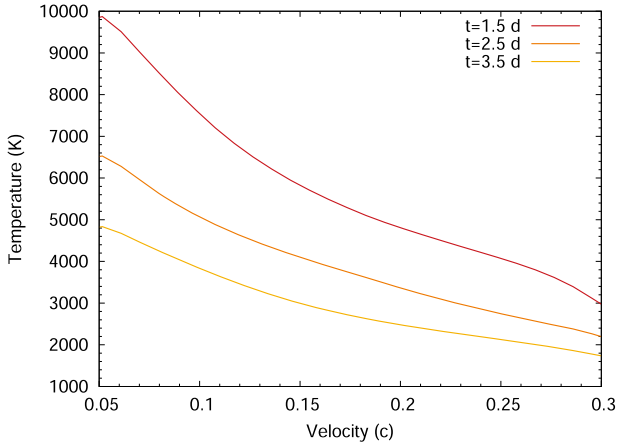

Figure 6. The temperature structure of the ejecta at $t = 1.5$, 2.5, and 3.5 days after the merger.

given by Barnes et al. (2016). The resulting temperature structure of the ejecta is shown in Figure 6.

3.2. Results

Figure 7 shows the synthetic spectrum at $t = 1.5$ days after the merger. To show the contribution of different elements, we also plot the Sobolev optical depths in the ejecta at $v = 0.16\,c$. The wavelengths of lines are blueshifted according to $v = 0.16\,c$. Note that we plot only spectroscopically accurate lines that contribute to absorption features.

The spectrum shows two strong absorption features at $\lambda \sim 8000$ Å (red arrow) and $\lambda \sim 6500$ Å (blue arrow). These are mainly caused by Sr II and Ca II as found in Domoto et al. (2021), although some Y II (dark-blue) and Zr II (green) lines also slightly affect the feature. In addition, the spectrum shows wide absorption features around $\lambda \sim 12{,}000$ and 14,000 Å (pink and orange arrows). These are produced by La III and Ce III lines, respectively. The presence of these absorption features is reasonable, because Ca II, Sr II, La III, and Ce III are found to be strong absorption sources in the one-zone analysis (Section 2). The central wavelengths of absorption lines for La III and Ce III show that the photospheric velocity at the NIR region is $v \sim 0.16c$, while that for Ca II and Sr II is $v \sim 0.2c$. This indicates that the line-forming regions for different wavelength ranges do not coincide owing to the wavelength-dependent opacity.

Figure 8 shows a comparison between our results and the observed spectra of AT2017gfo at $t = 1.5$, 2.5, and 3.5 days after the merger (Pian et al. 2017; Smartt et al. 2017; see Gillanders et al. 2022 for the latest calibration). We here focus only on the spectral features in the NIR region, because the absorption features by Ca and Sr in the observed spectra of AT2017gfo and their implication for the ejecta condition have already been discussed in Domoto et al. (2021). We find that the overall slopes of synthetic spectra in the NIR region are quite similar to the observed ones. The Doppler shift of absorption lines becomes smaller with time, because the density of the ejecta becomes lower and the photosphere moves inward (in mass coordinate). Interestingly, the positions of absorption features at the NIR wavelengths in our results are consistent with those seen in AT2017gfo, especially at $t \geqslant 2.5$ days. Although this model motivated by the observed luminosity of AT2017gfo is quite simple, the NIR features appear to agree with the observed ones without an adjustment

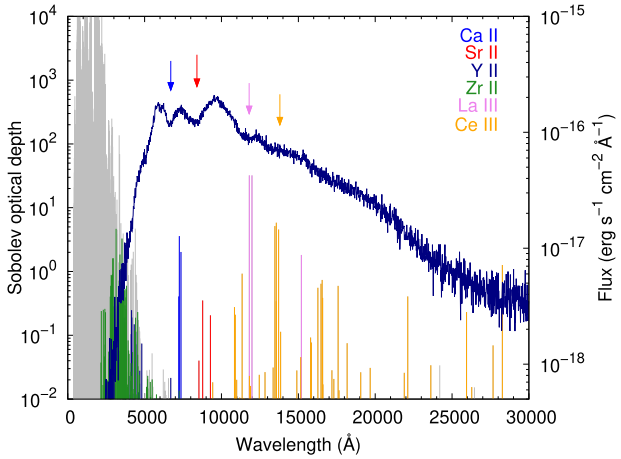

Figure 7. Synthetic spectrum (blue curve) and Sobolev optical depth of each transition (vertical lines) at $t = 1.5$ days. We plot the Sobolev optical depths of spectroscopically accurate lines in the ejecta at $v = 0.16\,c$. The positions of lines are blueshifted according to $v = 0.16\,c$. The temperature in the ejecta at $v = 0.16\,c$ is $T \sim 6000$ K.

of, e.g., density distribution. This implies that the absorption features at the NIR wavelengths in the spectra of AT2017gfo may be caused by the La III and Ce III lines.

It should be noted that the assumption of LTE may not be valid in a low-density region. In the results here, neutral atoms, especially for Y and Zr, which appear in the outer ejecta, are the dominant opacity sources at $t \geqslant 2.5$ days at the optical wavelengths (Tanaka et al. 2020; Kawaguchi et al. 2021; Gillanders et al. 2022). On the other hand, recent work on the nebula phase of kilonovae suggests that ionization fractions as well as the temperature structure of ejecta can be deviated from those expected in LTE with time, i.e., as the ejecta density decreases (Hotokezaka et al. 2021; Pognan et al. 2022b). These non-LTE effects may change the emergent spectra a few days after the merger, mainly at the optical wavelengths, where many strong lines of neutral atoms exist (Kawaguchi et al. 2021). Nevertheless, since the photosphere for the NIR region is located at the inner ejecta where the density is enough high, non-LTE effects are expected to be subdominant (Pognan et al. 2022a).

4. Discussion

4.1. Lanthanide Abundances

Our results show that kilonova photospheric spectra exhibit absorption features of La III and Ce III in the NIR region, which are in fact similar to those seen in the spectra of AT2017gfo. In this subsection, we examine a possible range of these lanthanide mass fractions in the ejecta of AT2017gfo by using the NIR features.

To investigate the effect of the La amount on the spectra, we perform the same simulations as in Section 3 but by varying the mass fraction of La. The resultant spectra at $t = 2.5$ days after the merger are shown in the left panel of Figure 9. We find that the strength of absorption due to the La III lines at $\lambda \sim 12500$ Å changes with the mass fraction of La. On the other hand, no matter how the mass fraction changes, the overall spectral shapes hardly change. Because La lines have little effect on the total opacity, the NIR opacity is almost unchanged. Thus, the strong lines of La III keep producing strong absorption as long as enough La is present. According to the tests shown in the left

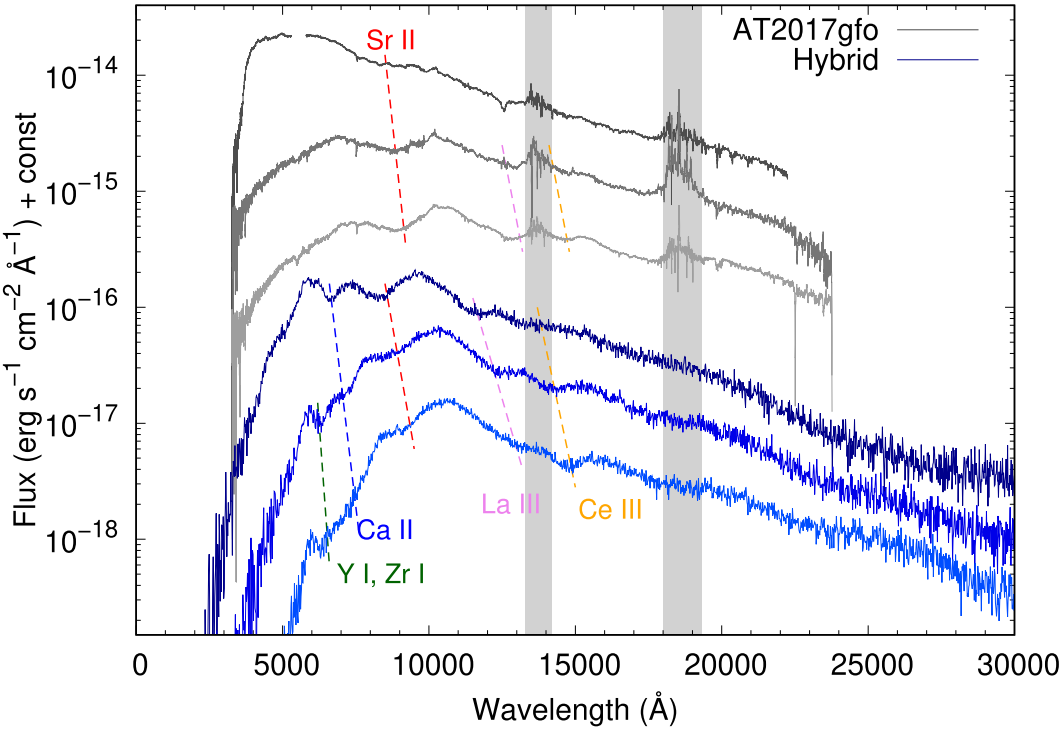

Figure 8. Comparison between the synthetic spectra (blue) and the observed spectra of AT2017gfo (gray, Pian et al. 2017; Smartt et al. 2017) at $t = 1.5$, 2.5, and 3.5 days after the merger (dark to light colors). Spectra are vertically shifted for visualization. The gray shade shows the regions of strong atmospheric absorption.

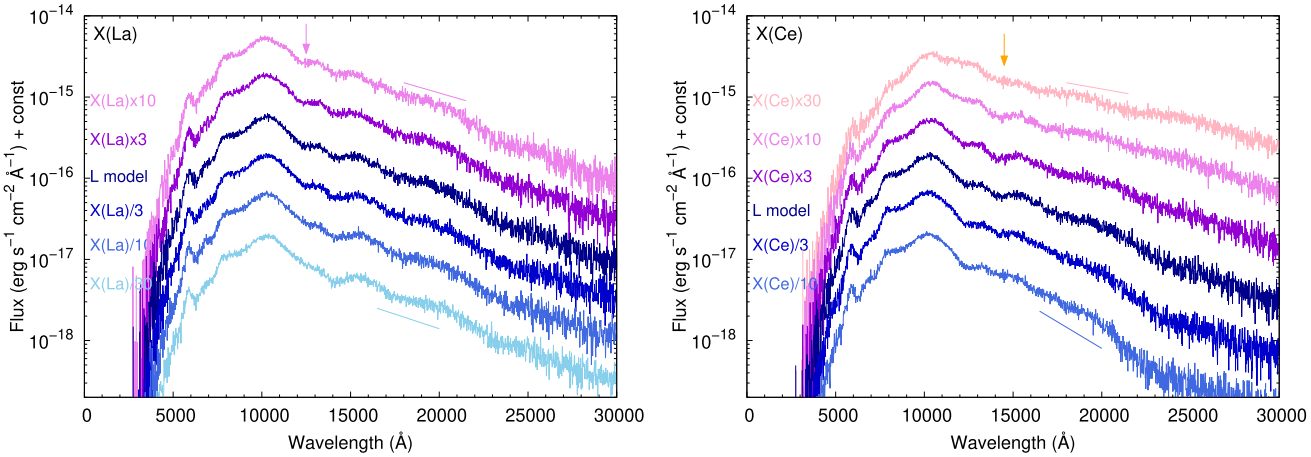

Figure 9. Synthetic spectra at $t = 2.5$ days after the merger for different mass fractions of La (left) and Ce (right). Variation of each element is shown in the legend with the same color used for the spectra. Pink and orange arrows in each panel indicate the position of the notable absorption lines caused by La III and Ce III, respectively. Line segments above and below the spectra indicate spectral slopes for visualization.

panel of Figure 9, we estimate that the mass fraction of La is higher than $1/30$ times that of the L model, i.e., $X(\mathrm{La}) > 2 \times 10^{-6}$, which is required to identify the visible absorption feature at $\lambda \sim 12500$ Å in the spectra of AT2017gfo.

By contrast, the situation is different in the case of Ce. To investigate the effect of the Ce amount on the spectra, we perform the same calculations for Ce as done for La above. The resultant spectra at $t = 2.5$ days after the merger are shown in the right panel of Figure 9. We find that the absorption feature at $\lambda \sim 14000$ Å diminishes as the mass fraction of Ce is substantially reduced (blueish curves). Also, the absorption feature disappears as well, even when the mass fraction of Ce is substantially increased (pink curve). Because Ce lines appreciably contribute to the total opacity, the higher Ce mass fraction results in a higher total opacity. As a result, the photosphere shifts outward compared to that in the L model. This makes the photospheric temperature lower, and thus, the Ce III lines disappear.

The amount of Ce affects not only absorption features but also overall spectral shapes. The spectra become redder and bluer when X(Ce) is increased and reduced, respectively. This is because Ce has high opacity in the NIR region and is the most dominant opacity source at the NIR wavelengths in this model. As the contribution of other heavy elements to the total opacity is subdominant, even if the mass fractions of all the elements with a mass number larger than 100 are varied by a factor of 10, the results are almost the same as those in the right panel of Figure 9. Note that the element species that dominate the opacity depend on the ejecta conditions (such as density, temperature, and epoch), but generally lanthanide elements

with a small atomic number (e.g., Ce and Nd) tend to have a larger contribution as they have more transitions from low-lying energy levels (Even et al. 2020; Tanaka et al. 2020).

We roughly estimate the mass fraction of Ce presented in the ejecta of AT2017gfo from our calculations. It is difficult to determine the exact amount of lanthanides from absorption features, because Ce has complex effects on spectral formation, as discussed above. Nevertheless, our demonstration suggests that a certain amount of Ce must have been present in order to explain the absorption features as well as the NIR fluxes. However, a too large amount of Ce diminishes the absorption features. As a result, the mass fraction of Ce is estimated to be between $1/3$ and 30 times that of the L model to account for the absorption feature, i.e., $X(\mathrm{Ce}) \sim (1\text{–}100) \times 10^{-5}$. This corresponds to the lanthanide mass fraction of $\sim(2\text{–}200) \times 10^{-4}$ if assuming the solar abundance pattern of *r*-process elements. While the lanthanide mass fraction estimated here is consistent with or somewhat higher than the values previously suggested (e.g., McCully et al. 2017; Nicholl et al. 2017; Gillanders et al. 2022), we emphasize that this is the first constraint on the lanthanide abundances using the absorption features in the spectra of AT2017gfo.

It should be noted that the results presented here are calculated with a single structure of ejecta (Section 3). The effects of ejecta properties, e.g., mass and velocity, on the spectra should be systematically examined. Furthermore, the spectra are calculated by assuming a simple one-dimensional morphology of ejecta with homogeneous abundance distribution. It is important to employ more realistic models to elucidate the effects of multidimensional ejecta structures. We leave such exploration to future work.

4.2. Features of Actinide Elements

We have shown that the ions that tend to produce absorption features in kilonova photospheric spectra can be explained by atomic properties (Section 2.2). According to the required properties, one can notice that not only lanthanides but also actinide elements can possibly contribute to the spectral features. However, while we include actinide elements in our abundance input up to $Z = 100$, actinide elements are not included in the line list due to the difficulty of atomic structure calculations for actinides (Tanaka et al. 2020). On the other hand, some experimental data are available for Th ($Z = 90$). In the following, we discuss the effects of Th absorption features based on experimental data.

Th III is one of the possible candidates for the ions that can contribute to the spectral features. The atomic structure of Th III is analogous to that of Ce III, which has two electrons in the outermost shell involving with *f*-shell. Fortunately, the energy levels of Th III are well established by experiments. For optical lines, not only transition wavelengths but also transition probabilities are available in the VALD database (Biémont et al. 2002). Moreover, the transition wavelengths in the NIR region are measured by experiments (Engleman 2003). However, there is no available data on transition probability for the NIR lines.

To test the possibility of identifying Th III lines in kilonova photospheric spectra, we estimate the transition probabilities of the NIR Th III lines by using the measured intensities. Since the relative intensities of the measured NIR lines (Engleman 2003) are listed in the NIST database (Kramida et al. 2021) in a consistent way with those of optical lines, we can directly compare the measured and calculated intensities for the lines over the whole wavelength range. Here, although the same estimate of *gf*-values can be, in principle, applicable to other ionization stages of Th, e.g., Th II, only those of Th III are tested. This is because lines of lower-ionized ions for Th are not expected to show strong transitions compared to those of Th III, such that Ce III show strong lines but Ce II does not (Section 2.2).

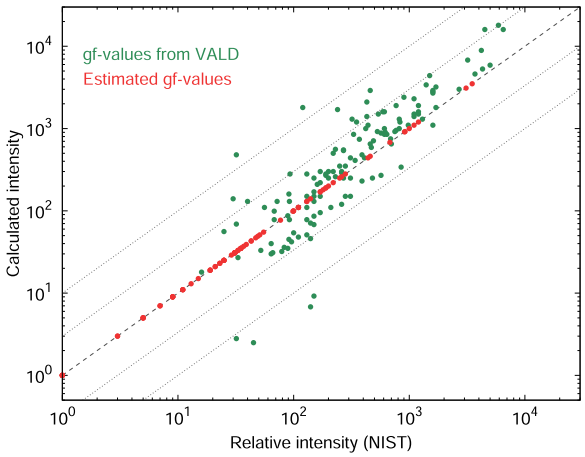

Figure 10. Comparison of intensities (green circles) for Th III lines between those calculated with *gf*-values from the VALD database and those measured by experiments (Kramida et al. 2021; Engleman 2003). Gray dashed and dotted lines correspond to perfect agreement and deviations by a factor of 3 and 10, respectively. Red circles indicate the lines whose *gf*-values are estimated from the measured intensities.

First, we calculate the line intensities for the optical lines for Th III with known *gf*-values taken from the VALD database using Equation (3). A comparison between the intensities calculated with the VALD *gf*-values and those measured by experiments for Th III (Kramida et al. 2021) is shown in Figure 10. We find that the calculated and experimentally measured intensities reasonably agree with each other when we adopt the temperature of $T = 5000$ K. Therefore, we estimate the transition probabilities of NIR lines for Th III by using the measured intensities (Engleman 2003; Kramida et al. 2021) and this temperature. Estimated *gf*-values are summarized in Table 5 (Appendix B).

Then, we calculate the strength of bound–bound transitions for Th III lines at $t = 1.5$ days for the L model, as in Section 2. The top panel of Figure 11 is the same as the bottom left panel of Figure 2 but with the Th III lines. We find that the strength of the Th III lines at the NIR wavelengths can be comparable to that of Ce III lines. This is due to the same reason as discussed in Section 2.2: relatively high transition probabilities and low energy levels of transitions.

We perform the same radiative transfer simulations as in Section 3 by including the Th III lines. The synthetic spectra with the Th III lines are shown in the bottom panel of Figure 11 (blue curves). We find that the fluxes for $\lambda \gtrsim 20000$ Å are slightly pushed up compared to those of the results without the Th III lines (light-blue curves, see Figure 8). However, the spectral features are not substantially different from those not including the Th III lines, although a wide and marginal absorption feature can be seen around $\lambda \sim 18000$ Å at $t = 1.5$ days. This implies that it is difficult to confirm the presence of Th from spectral features.

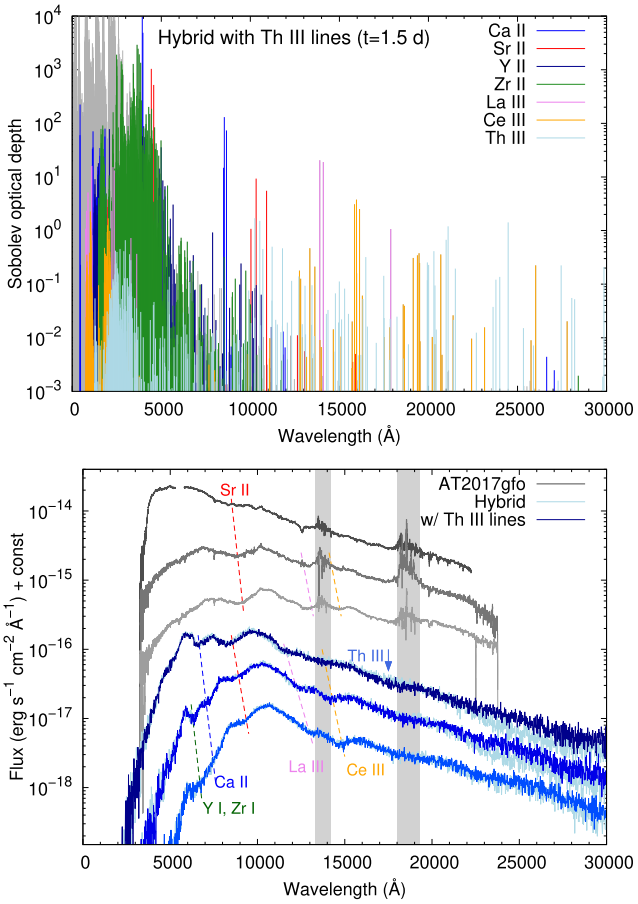

Figure 11. Top: Sobolev optical depth of bound–bound transitions calculated with the hybrid line list (Section 2.3) including Th III lines (light blue) taken from the VALD database ($\lambda < 10000$ Å) and the NIST database ($\lambda \geqslant 10000$ Å) at $t = 1.5$ days under the condition of $\rho = 10^{-14}$ g cm^{-3} and $T = 5000$ K. Bottom: comparison between the synthetic spectra including Th III lines (blue) and the observed spectra of AT2017gfo (gray, Pian et al. 2017; Smartt et al. 2017) at $t = 1.5$, 2.5, and 3.5 days after the merger (dark to light colors). The light-blue curves are the same as the blue curves in Figure 8.

The difference between the absorption features for Th III and Ce III can be explained by the complex atomic structure of actinides. As shown in the top panel of Figure 11, although the Th III lines in the NIR region are relatively strong, many transitions exhibit similar Sobolev optical depths and no significant line like that of Ce III at $\lambda \sim 16000$ Å exists. This is due to the fact that Th III has denser low-lying energy levels involved in 5*f*-shell compared to those of Ce III involved in 4*f*-shell. Silva et al. (2022) recently showed that the opacity of another actinide U III ($Z = 92$) is about an order of magnitude larger than that of Nd III for the same reason. Note that an actinide, Ac ($Z = 89$, as ^{227}Ac with the half-life of 21.77 yr), can also exist with a similar amount to those of Th and U in the ejecta of kilonovae. Ac III may have a similar atomic structure to that of La III. However, Ac III is poorly understood both in theory and experiments, and it is not clear if Ac III can produce prominent features like La III. Thus, although actinide ions can be important opacity sources in the NIR region, it may not be easy to identify the presence of actinides from the spectral features.

5. Conclusions

We have performed systematic calculations of the strength of bound–bound transitions and radiative transfer simulations with the aim of identifying elements in kilonova spectra. We constructed a hybrid line list by combining an experimentally calibrated accurate line list with a theoretically constructed complete line list. This allows us to investigate the entire wavelength range of kilonova photospheric spectra. We have found that La III and Ce III produce absorption features at the NIR wavelengths ($\lambda \sim 12000$–14000 Å). The positions of these features are consistent with those seen in the spectra of GW170817/AT2017gfo. Using the absorption lines caused by La III and Ce III, we have estimated that the mass fractions of La and Ce synthesized in the ejecta of GW170817/AT2017gfo are $X(\mathrm{La}) > 2 \times 10^{-6}$ and $X(\mathrm{Ce}) \sim (1\text{–}100) \times 10^{-5}$, respectively. This is the first spectroscopic estimation of the lanthanide abundances in NS merger ejecta.

We have shown that the elements on the left side of the periodic table (Ca, Sr, Y, Zr, Ba, La, and Ce) tend to produce prominent absorption features in kilonova photospheric spectra. This is due to the fact that such ions have a relatively small number of valence electrons in the outermost shell (leading to low complexities, and high transition probabilities for bound–bound transitions) and have relatively low-lying energy levels (leading to a large population in the Boltzmann distribution).

Since the atomic structure of Th III is analogous to that of Ce III, we have investigated the possibility of identifying Th III lines in kilonova spectra. We have found that it is more difficult to identify the definitive features caused by Th III, because it has denser low-lying energy levels and no outstanding identifiable lines. Although the atomic data of Th III (Table 5) are still uncertain, our demonstration suggests that we need to consider another way to obtain evidence of synthesized actinide elements from observables.

In this paper, we have used a model dominated by relatively light *r*-process elements. For more lanthanide-rich ejecta, the emergent spectra should be redder and fainter than predicted by our results, due to the high opacity of heavy elements. Also, the spectra should become smoother due to the presence of many weak lines from heavy elements. Since our hybrid line list is constructed assuming an abundance model dominated by light *r*-process elements, we are unable to discuss spectral features in the lanthanide-rich ejecta. To extract more information from various spectra, further effort is necessary to construct spectroscopically accurate atomic data for heavy elements. It is also cautioned that the abundance with $Z \leqslant 19$ has been excluded in our calculations, because their mass fractions are very small ($<10^{-4}$) except for He (the left panel of Figure 1). Although He might produce absorption features in spectra, it requires the consideration of non-LTE effects on the level population (Perego et al. 2022). While the exclusion of light elements does not affect our conclusions under the assumption of LTE, the systematic exploration of He line formation will be of interest in the future.

Part of the numerical simulations presented in this paper was carried out on Cray XC50 at the Center for Computational Astrophysics, National Astronomical Observatory of Japan. N.D. acknowledges support from Graduate Program on Physics for the Universe (GP-PU) at Tohoku University. This research was supported by NIFS Collaborative Research Program (NIFS22KIIF005), the Grant-in-Aid for JSPS Fellows (22J22810), the Grant-in-Aid for Scientific Research from JSPS (19H00694, 20H00158, 21H04997, 21K13912), and MEXT (17H06363).

Appendix A
Calibration of Atomic Data

We calibrate the theoretical atomic data with experimental data to enable us to discuss absorption lines in kilonova spectra. Here, we describe our method of this calibration procedure. We perform the calibration for Sr II, Y I, Y II, Zr I, Zr II, Ba II, La III, and Ce III, which are found as strong absorption sources in Section 2.1. For the experimental data, we use the NIST Atomic Spectra Database (Kramida et al. 2021) to calibrate the energy levels. The energy levels of these ions have been well determined from experiments mainly in the optical wavelengths.

The NIST database lists term symbols of energy levels. By using those symbols, it is possible to associate the theoretical energy levels with those in the NIST database. It should be, however, noted that energy terms can be expressed in different ways depending on angular momentum coupling schemes: LS-coupling and jj-coupling. While the NIST database adopts the LS scheme, the HULLAC code used for atomic calculations adopts the jj scheme (Bar-Shalom et al. 2001). Since it is not possible to directly compare energy levels in different schemes, we perform the transformation from the jj-coupled to the LS-coupled energy terms for the theoretical energy levels (Cowan 1968, 1981).

While energy terms are uniquely determined for one-electron systems (Sr II, Ba II, and La III), transformations are required for atoms with more than two valence electrons. To perform all the transformations systematically, we use the LSJ code (Gaigalas et al. 2004). The LSJ code transforms a jj-coupled basis to an LS-coupled representation according to inputs of configuration state functions (CSF) and mixing coefficients. For the input of the LSJ code, we prepare the CSF lists for each ion by means of GRASP2018 (Froese Fischer et al. 2019) and mixing coefficients for energy levels from the HULLAC results (Tanaka et al. 2020). Using these inputs, we perform the jj-LS transformations for the energy levels of Y I, Y II, Zr I, Zr II, and Ce III.

As an energy term for each energy level, we assign the leading term with the largest mixing coefficient from the results of the LSJ code. When leading terms are the same for two levels, we assign the term to a level with a larger mixing coefficient than the other one. For the other level, the unassigned term with the next largest coefficient is assigned.

For the spectral features or opacity of kilonovae, calibration of low-lying energy levels is the most important (Section 2.2). Nevertheless, we also perform the transformation for many excited levels so that we have enough transitions to confirm the accuracy of *gf*-values (see below, the right panels of Figures 12–19). Since ions with a smaller number of valence electrons tend to have a smaller number of levels, we perform the calibration for a larger number of configurations for simpler ions. As a result, our calibrated line list naturally includes strong and important transitions. The energy diagrams of calibrated configurations for each ion are shown in the left panels of Figures 12–19.

For Zr I, the calibration is performed in a slightly different way from other ions. When angular momenta of more than three electrons are coupled, intermediate terms are needed to distinguish the energy terms. However, for the energy terms of most levels in $4d^2 5s5p$ for Zr I, the NIST database shows the intermediate terms in a different way from the LSJ code. Therefore, we associate the energy terms for $4d^2 5s5p$ of the HULLAC results and the NIST database in the order of energy among levels with the same total angular momentum J.

After calibration of the energy levels, we calibrate the wavelengths of the transitions between the calibrated energy levels. Since we aim to discuss the spectral features of kilonovae, the lines whose original and calibrated wavelengths are in the forest of lines at $\lambda < 5000$ Å are left as the original theoretical ones for simplicity. Then, if available, transition probabilities of the calibrated lines are taken from the VALD database (Piskunov et al. 1995; Kupka et al. 1999; Ryabchikova et al. 2015). For Zr I and Zr II, we instead use Kurucz's atomic data[11] (Kurucz 2018), which are constructed by semiempirical calculations and newer than those in the VALD database. We use these databases instead of the NIST database, because the NIST database does not necessarily include all the transition data for heavy elements. If the transition probabilities of the calibrated lines are not listed in both databases, we adopt those from the theoretical calculations, which only happens to La III and Ce III mainly in NIR wavelengths. We summarize the calibrated lines that adopt the theoretical *gf*-values with $\lambda > 7000$ Å and $\log gf > -3$ in Tables 3–4.

Note that, theoretically calculated transition probabilities are not necessarily accurate. The right panels of Figures 12–19 show a comparison of *gf*-values between the HULLAC results and the VALD (or Kurucz's) database for all the lines between the calibrated energy levels. We see that, while the values roughly agree for simple ions, there is a scatter as the number of outermost electrons increases, especially for low *gf*-values. This is unavoidable, as the theoretical calculations become inaccurate as atomic structures become complex. Nevertheless, it is emphasized that the uncertainty of theoretical *gf*-values does not affect our conclusions about NIR spectral features, because *gf*-values of La III and Ce III agree quite well for strong transitions as shown in the right panel of Figures 18 and 19 (see also Figure 5 for the NIR Ce III lines). To determine the exact values of transition probabilities of the lines, more experimental and observational calibrations are necessary.

[11] http://kurucz.harvard.edu/atoms.html

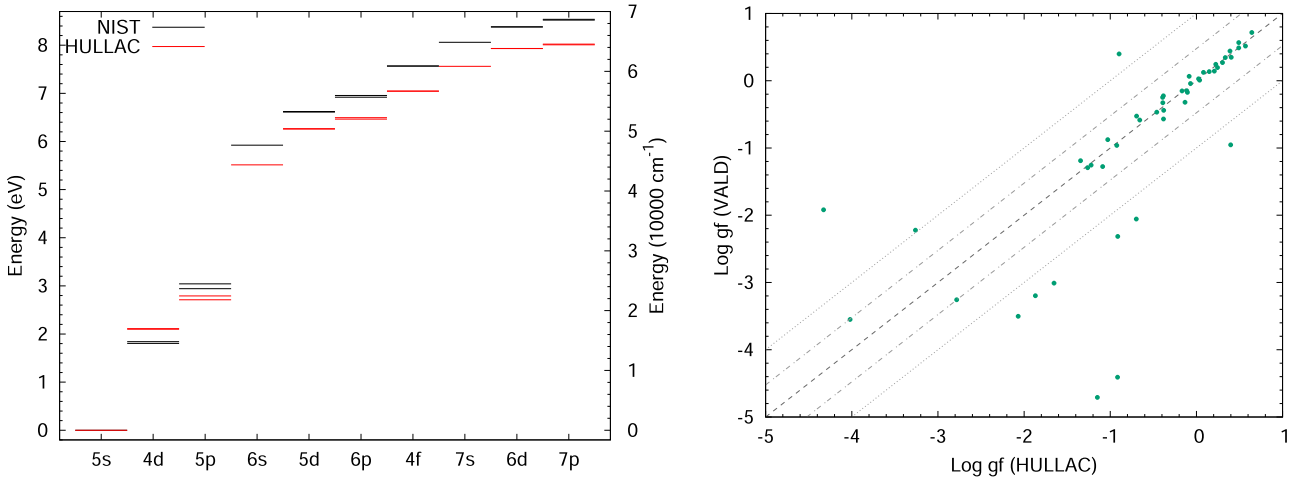

Figure 12. Left: energy diagram for Sr II. Black and red lines show energy levels from the NIST database and the HULLAC results, respectively. Right: comparison of *gf*-values between the VALD database and the HULLAC results. Gray dashed line corresponds to perfect agreement between them, and dashed–dotted and dotted lines indicate deviations by a factor of 3 and 10, respectively.

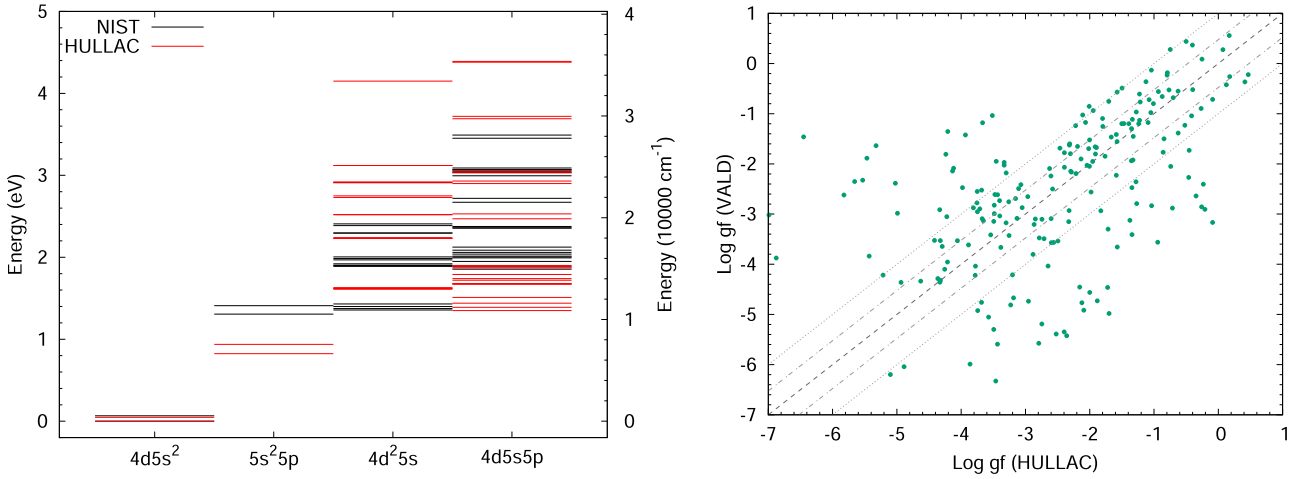

Figure 13. Same as Figure 12, but for Y I.

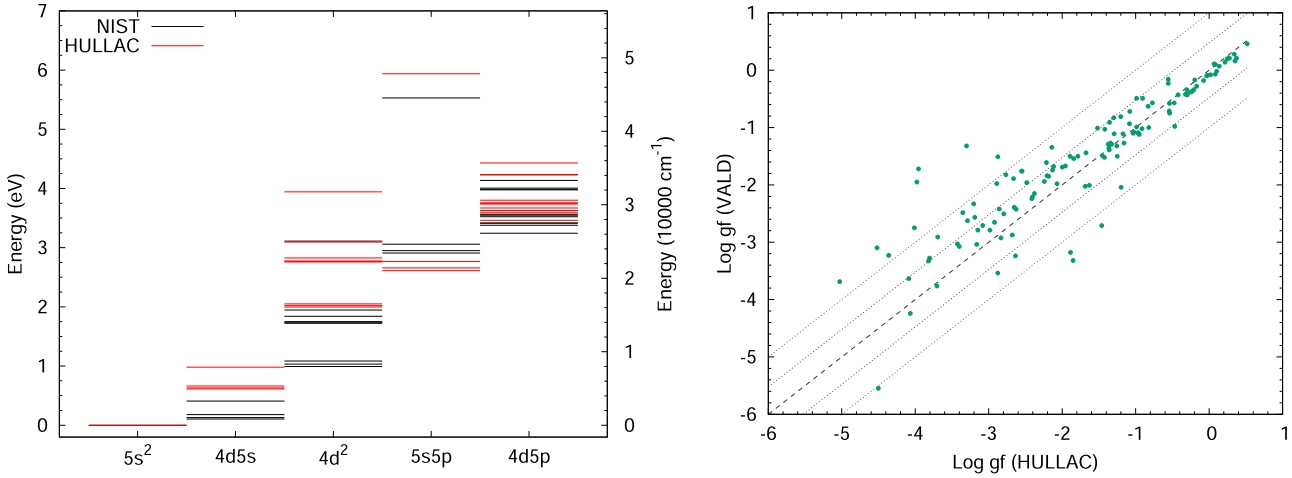

Figure 14. Same as Figure 12, but for Y II.

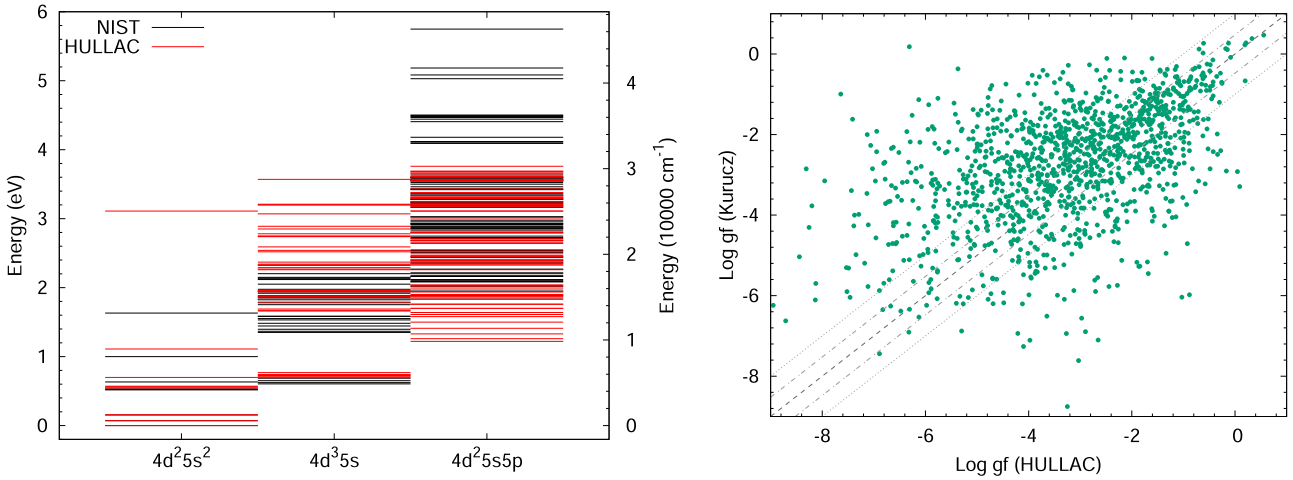

Figure 15. Same as Figure 12, but for Zr I. Kurucz's atomic data are used instead of the VALD database for comparison in the right panel. The energy levels of $4d^2 5s5p$ above 4 eV for the HULLAC results are not shown and not used for the calibration because of strong mixing with high-lying levels of other configurations.

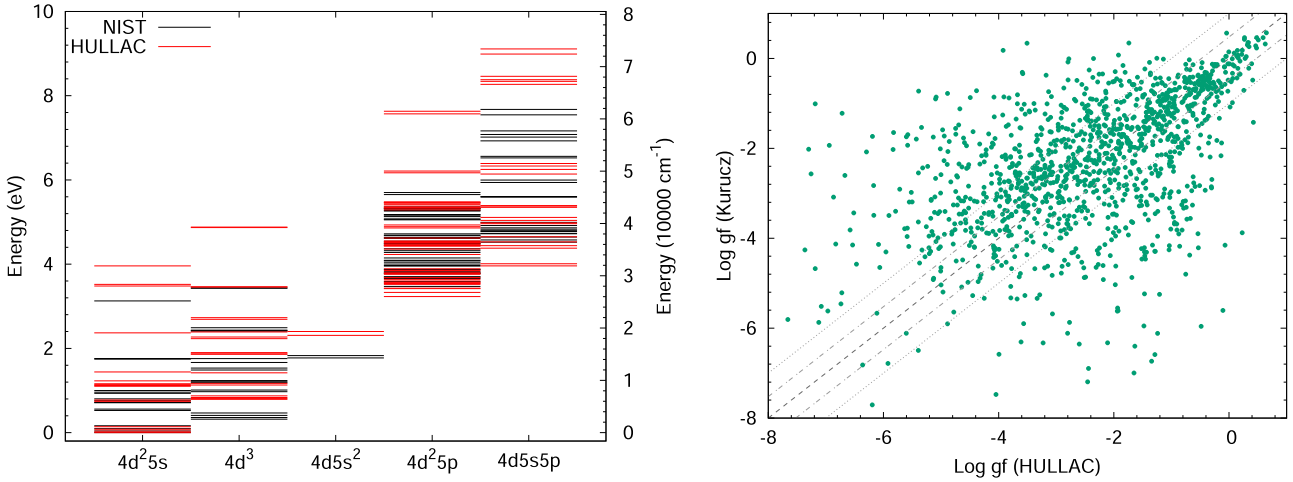

Figure 16. Same as Figure 12, but for Zr II. Kurucz's atomic data are used instead of the VALD database for comparison in the right panel.

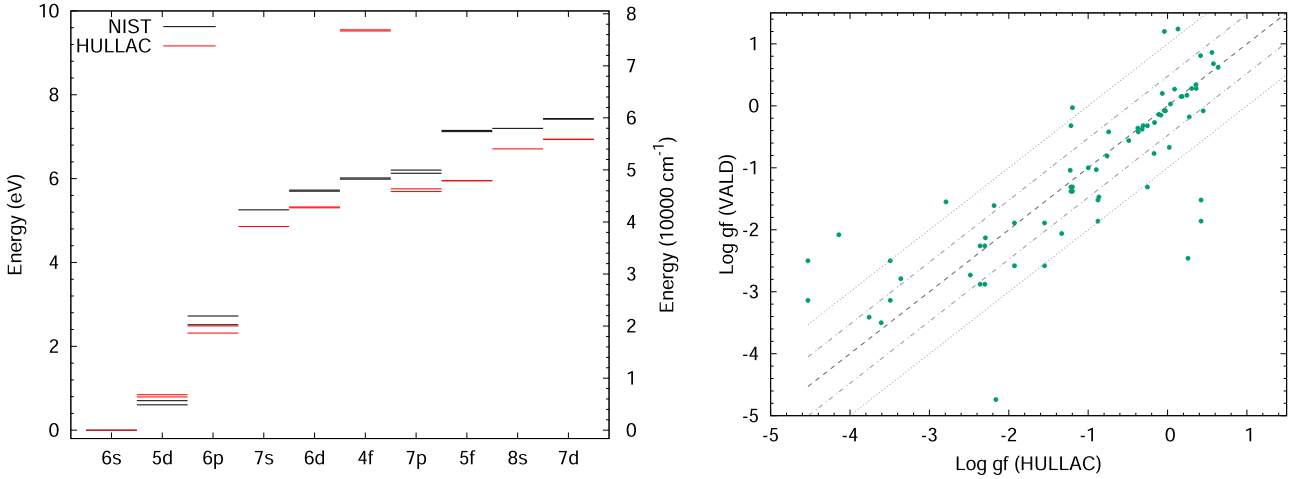

Figure 17. Same as Figure 12, but for Ba II.

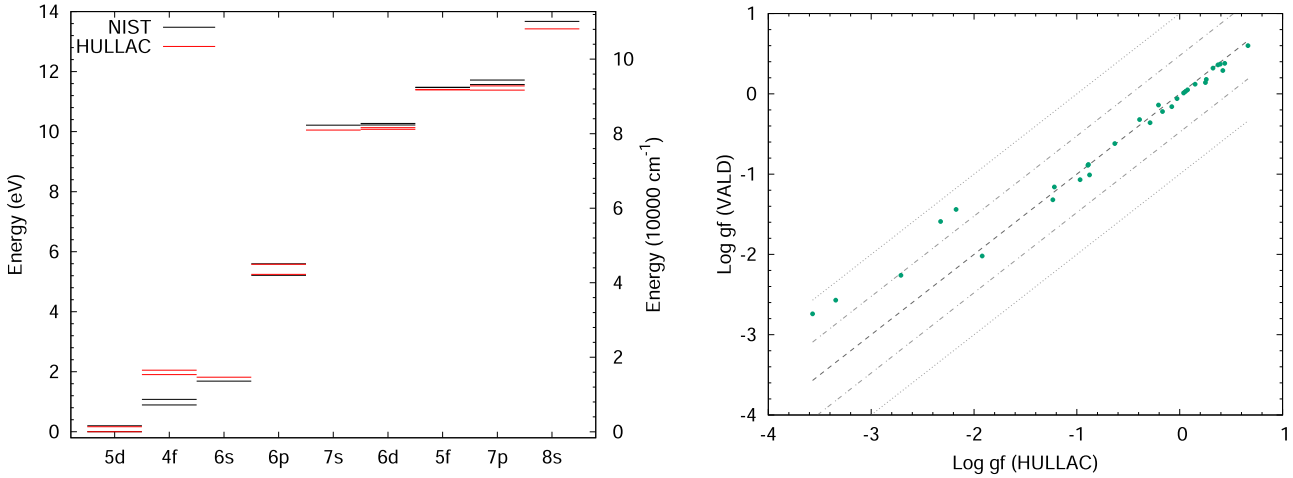

Figure 18. Same as Figure 12, but for La III.

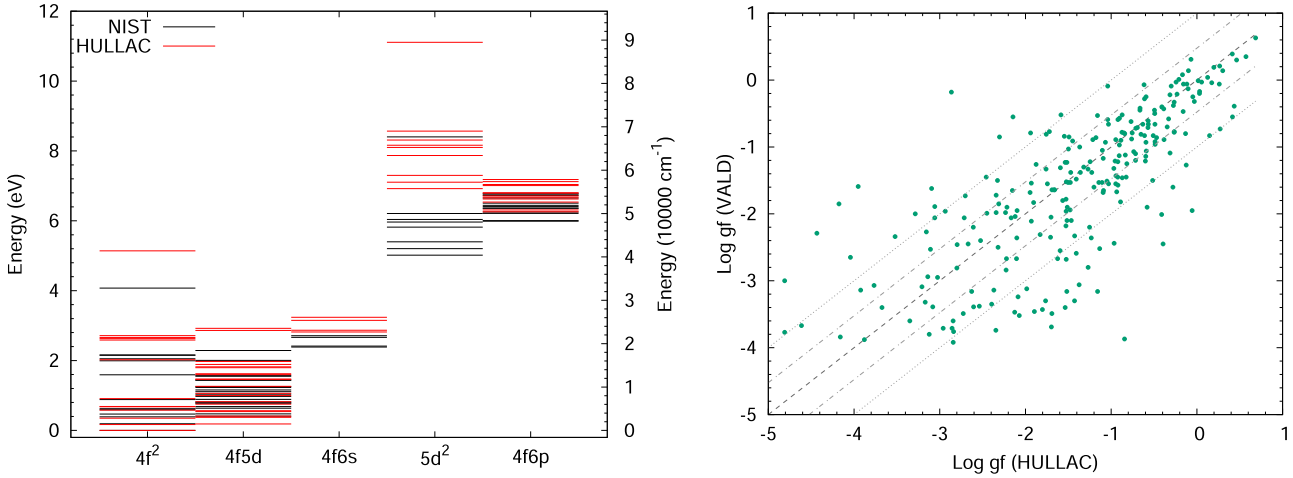

Figure 19. Same as Figure 12, but for Ce III.

Table 3
Summary of Calibrated Lines for La III

	λ_{vac}[a] (Å)	λ_{air}[b] (Å)	Lower Level	E_{lower}[c] (cm^{-1})	Upper Level	E_{upper}[d] (cm^{-1})	log gf[e]
La III	13898.270	13894.471	$5d\ ^2D_{3/2}$	0.00	$4f\ ^2F^o_{5/2}$	7195.14	−0.749
	14100.037	14096.183	$5d\ ^2D_{5/2}$	1603.23	$4f\ ^2F^o_{7/2}$	8695.41	−0.587
	17882.977	17878.094	$5d\ ^2D_{5/2}$	1603.23	$4f\ ^2F^o_{5/2}$	7195.14	−1.938

Notes. We list only lines that adopt theoretical *gf*-values with $\lambda > 7000$ Å and log $gf > -3$.
[a] Vacuum transition wavelength.
[b] Air transition wavelength.
[c] Lower energy level.
[d] Upper energy level.
[e] *gf*-value (Tanaka et al. 2020).

Table 4
Same as Table 3, but for Ce III

	λ_{vac} [a] (Å)	λ_{air} [b] (Å)	Lower Level	E_{lower} [c] (cm^{-1})	Upper Level	E_{upper} [d] (cm^{-1})	log gf [e]
Ce III	8100.800	8098.573	$4f^2\ ^1G_4$	7120.000	$4f6s\left(\frac{5}{2}\frac{1}{2}\right)_3$	19464.460	−2.682
	11071.353	11068.321	$4f^2\ ^1G_4$	7120.000	$4f5d\ ^1H_5^o$	16152.320	−2.636
	11093.386	11090.349	$4f^2\ ^1D_2$	12835.090	$4f6s\left(\frac{7}{2}\frac{1}{2}\right)_3$	21849.470	−2.870
	11094.396	11091.358	$4f5d\ ^3F_2^o$	3821.530	$4f^2\ ^1D_2$	12835.090	−2.669
	12760.441	12756.951	$4f^2\ ^3H_4$	0.000	$4f5d\ ^3G_4^o$	7836.720	−1.947
	12825.133	12821.626	$4f^2\ ^3H_5$	1528.320	$4f5d\ ^3G_5^o$	9325.510	−1.910
	12926.644	12923.109	$4f^2\ ^3F_3$	4764.760	$4f5d\ ^1F_3^o$	12500.720	−2.598
	13155.108	13151.511	$4f5d\ ^3D_1^o$	8922.050	$4f^2\ ^3P_1$	16523.660	−2.454
	13342.833	13339.185	$4f^2\ ^3F_4$	5006.060	$4f5d\ ^1F_3^o$	12500.720	−0.922
	13482.540	13478.854	$4f5d\ ^3D_2^o$	9900.490	$4f^2\ ^3P_2$	17317.490	−2.368
	13906.349	13902.548	$4f5d\ ^3D_3^o$	10126.530	$4f^2\ ^3P_2$	17317.490	−2.014
	13986.034	13982.211	$4f5d\ ^3D_1^o$	8922.050	$4f^2\ ^3P_0$	16072.040	−2.298
	14659.167	14655.161	$4f^2\ ^3H_5$	1528.320	$4f5d\ ^3H_6^o$	8349.990	−2.911
	15098.510	15094.385	$4f5d\ ^3D_2^o$	9900.490	$4f^2\ ^3P_1$	16523.660	−2.013
	15720.131	15715.837	$4f^{23}H_4$	0.000	$4f5d\ ^3H_5^o$	6361.270	−2.985
	15851.880	15847.550	$4f^2\ ^3H_5$	1528.320	$4f5d\ ^3G_4^o$	7836.720	−0.613
	15961.157	15956.797	$4f^2\ ^3H_4$	0.000	$4f5d\ ^3G_3^o$	6265.210	−0.721
	15964.928	15960.567	$4f5d\ ^1D_2^o$	6571.360	$4f^2\ ^1D_2$	12835.090	−1.272
	16133.170	16128.763	$4f^2\ ^3H_6$	3127.100	$4f5d\ ^3G_5^o$	9325.510	−0.509
	16292.642	16288.192	$4f^2\ ^3F_2$	3762.750	$4f5d\ ^3D_2^o$	9900.490	−2.050
	17529.037	17524.251	$4f5d\ ^3P_1^o$	11612.670	$4f^2\ ^3P_2$	17317.490	−1.873
	17829.952	17825.084	$4f^2\ ^1D_4$	12835.090	$4f5d\ ^1P_1^o$	18443.630	−1.546
	18584.873	18579.800	$4f^2\ ^1G_4$	7120.000	$4f5d\ ^1F_3^o$	12500.720	−1.850
	18650.558	18645.466	$4f^2\ ^3F_3$	4764.760	$4f5d\ ^3D_3^o$	10126.530	−2.173
	19146.488	19141.261	$4f^2\ ^3H_6$	3127.100	$4f5d\ ^3H_6^o$	8349.990	−1.496
	19382.474	19377.184	$4f^2\ ^3F_2$	3762.750	$4f5d\ ^3D_1^o$	8922.050	−1.373
	19471.429	19466.114	$4f^2\ ^3F_3$	4764.760	$4f5d\ ^3D_2^o$	9900.490	−1.210
	19503.556	19498.233	$4f^2\ ^3H_4$	0.000	$4f5d\ ^3H_4^o$	5127.270	−1.987
	19529.457	19524.127	$4f^2\ ^3F_4$	5006.060	$4f5d\ ^3D_3^o$	10126.530	−2.825
	20216.315	20210.797	$4f5d\ ^3P_0^o$	11577.160	$4f^2\ ^3P_1$	16523.660	−1.937
	20362.493	20356.936	$4f5d\ ^3P_1^o$	11612.670	$4f^2\ ^3P_1$	16523.660	−2.072
	20691.296	20685.649	$4f^2\ ^3H_5$	1528.320	$4f5d\ ^3H_5^o$	6361.270	−1.665
	20760.800	20755.135	$4f5d\ ^1F_3^o$	12500.720	$4f^2\ ^3P_2$	17317.490	−2.167
	21386.074	21380.238	$4f5d\ ^3P_2^o$	12641.550	$4f^2\ ^3P_2$	17317.490	−1.426
	22424.692	22418.574	$4f5d\ ^3P_1^o$	11612.670	$4f^{23}P_0$	16072.040	−2.010
	23151.096	23144.779	$4f^2\ ^3F_4$	5006.060	$4f5d\ ^3G_5^o$	9325.510	−2.639
	25759.188	25752.161	$4f5d\ ^3P_2^o$	12641.550	$4f^2\ ^3P_1$	16523.660	−1.972
	26019.036	26011.938	$4f5d\ ^1G_4^o$	3276.660	$4f^2\ ^1G_4$	7120.000	−1.749

Notes. We list only lines that adopt theoretical gf-values with $\lambda > 7000$ Å and log $gf > -3$.
[a] Vacuum transition wavelength.
[b] Air transition wavelength.
[c] Lower energy level.
[d] Upper energy level.
[e] gf-value (Tanaka et al. 2020).

Appendix B
Estimated Transition Probabilities of Th III Lines

We summarize the *gf*-values of Th III lines estimated by using the measured line intensities in Table 5 (see Section 4.2).

Table 5
Summary of Lines for Th III

	λ_{vac}[a] (Å)	λ_{air}[b] (Å)	Lower Level	E_{lower}[c] (cm^{-1})	Upper Level	E_{upper}[d] (cm^{-1})	log *gf*[e]
Th III	10046.6354	10043.8823	$5f6d\ ^3H^o_4$	0.000	$6d7s\ ^3D_3$	9953.581	−1.984
	10257.0203	10254.2105	$5f6d$	6288.221	$6d7s\ ^1D_2$	16037.641	−1.106
	10260.9778	10258.1662	$5f6d\ ^3G^o_4$	8141.749	$5f^2\ ^3H_5$	17887.409	0.979
	10532.8695	10529.9844	$5f6d\ ^3G^o_5$	11276.807	$5f^2\ ^3H_6$	20770.896	1.310
	10581.3571	10578.4585	$5f6d\ ^3H^o_6$	8436.826	$5f^2\ ^3H_5$	17887.409	−0.994
	10710.5316	10703.6448	$5f6d\ ^1H^o_5$	19009.910	$5f^2\ ^1I_6$	28349.962	1.744
	11216.3023	11213.2319	$6d^2\ ^3F_4$	6537.817	$5f6d\ ^1F^o_3$	15453.412	−0.796
	11227.3116	11224.2381	$5f6d$	8980.557	$5f^2\ ^3H_5$	17887.409	0.513
	11428.8103	11425.6824	$7s^2\ ^1S_0$	11961.132	$5f6d\ ^1P^o_1$	20710.949	−0.485
	11516.6200	11513.4678	$5f6d\ ^3D^o_2$	10180.766	$5f^2\ ^3F_2$	18863.869	−0.799
	11720.8814	11717.6743	$6d^2$	4676.432	$5f6d\ ^3P^o_2$	13208.214	−1.637
	11810.5436	11807.3118	$6d^2\ ^1G_4$	10542.899	$5f6d\ ^1H^o_5$	19009.910	0.657
	12081.2271	12077.9218	$6d7s\ ^3D_2$	7176.107	$5f6d\ ^1F^o_3$	15453.412	−1.159
	12320.5004	12317.1299	$5f6d\ ^3D^o_1$	7921.088	$6d7s\ ^1D_2$	16037.641	−0.295
	12726.1743	12722.6938	$6d^2\ ^3F_2$	63.267	$5f6d\ ^3D^o_1$	7921.088	−1.209
	12918.7449	12915.2129	$5f6d\ ^3P^o_1$	11123.179	$5f^2\ ^3F_2$	18863.869	−0.724
	13075.4606	13071.8856	$5f7s$	7500.605	$5f^2\ ^3H_4$	15148.519	−0.466
	13102.2536	13098.6709	$5f6d\ ^3P^o_2$	13208.214	$5f^2\ ^3F_3$	20840.489	−0.661
	13445.6702	13441.9943	$6d^2\ ^3F_2$	63.267	$5f7s$	7500.605	−2.137
	13465.3195	13461.6378	$5f7s$	2527.095	$6d7s\ ^3D_3$	9953.581	−1.090
	13577.6105	13573.8997	$5f6d\ ^3F^o_2$	510.758	$6d^2\ ^3P_1$	7875.824	−2.619
	13596.9369	13593.2186	$5f6d$	3188.301	$6d^2\ ^1G_4$	10542.899	−1.960
	14271.9111	14268.0108	$5f6d\ ^3G^o_4$	8141.749	$5f^2\ ^3H_4$	15148.519	−0.949
	14363.1448	14359.2200	$5f6d\ ^1H^o_5$	19009.910	$5f^2\ ^1G_4$	25972.173	0.478
	14766.5150	14762.4802	$5f7s\ ^3F^o_2$	3181.502	$6d7s\ ^3D_3$	9953.581	−2.286
	14781.3544	14777.3154	$5f6d$	3188.3016	$d7s\ ^3D_3$	9953.581	−1.198
	14958.5620	14954.4750	$6d^2\ ^3F_3$	4056.015	$5f6d\ ^3D^o_3$	10741.150	−1.640
	15002.9667	14998.8674	$5f6d\ ^3F^o_2$	510.758	$6d7s\ ^3D_2$	7176.107	−1.319
	15127.2149	15123.0814	$5f6d\ ^3G^o_5$	11276.807	$5f^2\ ^3H_5$	17887.409	−0.684
	15295.6248	15291.4461	$5f6d\ ^3H^o_4$	0.000	$6d^2\ ^3F_4$	6537.817	−1.523
	15511.6993	15507.4618	$6d^2$	4676.432	$5f6d\ ^3P^o_0$	11123.179	−1.418
	16064.3747	16059.9860	$6d^2\ ^3F_2$	63.267	$5f6d$	6288.221	−2.781
	16212.8109	16208.3834	$5f6d$	8980.557	$5f^2\ ^3H_4$	15148.519	−1.665
	16327.1959	16322.7369	$6d^2\ ^3F_3$	4056.015	$5f6d\ ^3D^o_2$	10180.766	−1.239
	16488.8131	16484.3100	$6d^2$	4676.432	$5f6d\ ^3D^o_3$	10741.150	−0.384
	16577.9550	16573.4271	$6d7s\ ^3D_2$	7176.107	$5f6d\ ^3P^o_2$	13208.214	−1.372
	17073.9505	17069.2888	$5f6d\ ^3D^o_2$	10180.766	$6d7s\ ^1D_2$	16037.641	−1.313
	17494.5296	17489.7524	$5f6d$	4826.826	$6d^2\ ^1G_4$	10542.899	−0.741
	17517.0190	17512.2353	$6d7s\ ^3D_1$	5523.881	$5f6d\ ^3P^o_0$	11232.615	−1.441
	17814.4804	17809.6160	$5f6d$	4826.826	$6d^2\ ^3P_2$	10440.237	−2.318
	17859.3810	17854.5071	$6d7s\ ^3D_1$	5523.881	$5f6d\ ^3P^o_1$	11123.179	−1.467
	18182.3784	18177.4150	$6d7s\ ^3D_3$	9953.581	$5f6d\ ^1F^o_3$	15453.412	−2.372
	18240.3369	18235.3613	$5f6d\ ^3G^o_3$	5060.544	$6d^2\ ^1G_4$	10542.899	−1.492
	18588.4201	18583.3460	$5f6d\ ^3G^o_3$	5060.544	$6d^2\ ^3P_2$	10440.237	−2.281
	18880.4240	18875.2700	$5f6d\ ^3D^o_3$	10741.150	$6d7s\ ^1D_2$	16037.641	−1.312
	19947.4412	19941.9969	$6d^2\ ^3P_2$	10440.237	$5f6d\ ^1F^o_3$	15453.412	−0.178
	19947.6467	19942.2025	$5f6d\ ^3F^o_2$	510.758	$6d7s\ ^3D_1$	5523.881	−1.086
	20010.8977	20005.4362	$6d^2\ ^3F_2$	63.267	$5f6d\ ^3G^o_3$	5060.544	−1.190
	20306.4569	20300.9148	$6d^2\ ^3F_3$	4056.015	$5f6d$	8980.557	−0.442
	20364.4720	20358.9157	$6d^2\ ^1G_4$	10542.899	$5f6d\ ^1F^o_3$	15453.412	−0.274
	20437.2044	20431.6273	$5f6d\ ^3G^o_3$	5060.544	$6d7s\ ^3D_3$	9953.581	−1.782
	20992.7055	20986.9762	$6d^2\ ^3F_2$	63.267	$5f6d$	4826.826	−0.743

Table 5
(Continued)

λ_{vac}[a] (Å)	λ_{air}[b] (Å)	Lower Level	E_{lower}[c] (cm^{-1})	Upper Level	E_{upper}[d] (cm^{-1})	log gf[e]
21101.5437	21095.7851	$6d^2\ ^3F_4$	6537.817	$5f6d\ ^3G^o_5$	11276.807	0.314
21398.1215	21392.2817	$6d7s\ ^1D_2$	16037.641	$5f6d\ ^1P^o_1$	20710.949	−0.251
21473.5815	21467.7282	$6d7s\ ^3D_1$	5523.881	$5f6d\ ^3D^o_2$	10180.766	−2.887
21509.9507	21504.0820	$5f7s$	2527.095	$6d7s^3D_2$	7176.107	−0.982
22689.2716	22683.0812	$5f6d\ ^3D^o_3$	10741.150	$5f^2\ ^3H_4$	15148.519	−1.177
23628.9815	23622.5344	$5f7s\ ^3F^o_4$	6310.808	$6d^2\ ^1G_4$	10542.899	−1.267
23790.6455	23784.1542	$6d^2\ ^3F_4$	6537.817	$5f6d\ ^3D^o_3$	10741.150	−0.732
24005.7196	23999.1688	$5f6d\ ^3F^o_2$	510.758	$6d^2$	4676.432	−1.437
24475.4075	24468.7299	$6d^2\ ^3F_3$	4056.015	$5f6d\ ^3G^o_4$	8141.749	0.013
25335.2327	25328.3228	$6d7s\ ^3D_2$	7176.107	$5f6d\ ^3P^o_1$	11123.179	−1.584
25897.4091	25890.3447	$5f^2\ ^3H_4$	15148.519	$5f6d\ ^1H^o_5$	19009.910	−0.921
27282.4514	27275.0145	$5f6d$	6288.221	$6d7s\ ^3D_3$	9953.581	−2.707
27451.6126	27444.1264	$5f7s\ ^3F^o_4$	6310.808	$6d7s\ ^3D_3$	9953.581	−0.556
28050.1492	28042.4984	$6d7s\ ^3D_2$	7176.107	$5f6d\ ^3D^o_3$	10741.150	−1.066
28206.6978	28199.0038	$5f6d\ ^3F^o_2$	510.758	$6d^2\ ^3F_3$	4056.015	−1.924
29790.3617	29782.2484	$6d^2\ ^3P_1$	7875.824	$5f6d\ ^3P^o_0$	11232.615	−2.471
29855.0580	29846.9168	$5f6d$	3188.301	$6d^2\ ^3F_4$	6537.817	−1.015

Notes. *gf*-values are estimated from the measured line intensities.
[a] Vacuum transition wavelength.
[b] Air transition wavelength.
[c] Lower energy level.
[d] Upper energy level.
[e] *gf*-value estimated in Section 4.2.

ORCID iDs

Nanae Domoto https://orcid.org/0000-0002-7415-7954
Masaomi Tanaka https://orcid.org/0000-0001-8253-6850
Daiji Kato https://orcid.org/0000-0002-5302-073X
Kyohei Kawaguchi https://orcid.org/0000-0003-4443-6984
Kenta Hotokezaka https://orcid.org/0000-0002-2502-3730
Shinya Wanajo https://orcid.org/0000-0002-4759-7794

References

Abbott, B. P., Abbott, R., Abbott, T. D., et al. 2017a, PhRvL, 119, 161101
Abbott, B. P., Abbott, R., Abbott, T. D., et al. 2017b, ApJL, 848, L12
Arcavi, I., Hosseinzadeh, G., Howell, D. A., et al. 2017, Natur, 551, 64
Banerjee, S., Tanaka, M., Kawaguchi, K., Kato, D., & Gaigalas, G. 2020, ApJ, 901, 29
Barnes, J., & Kasen, D. 2013, ApJ, 775, 18
Barnes, J., Kasen, D., Wu, M.-R., & Martínez-Pinedo, G. 2016, ApJ, 829, 110
Bar-Shalom, A., Klapisch, M., & Oreg, J. 2001, JQSRT, 71, 169
Biémont, E., Palmeri, P., Quinet, P., Zhang, Z. G., & Svanberg, S. 2002, ApJ, 567, 1276
Coulter, D. A., Foley, R. J., Kilpatrick, C. D., et al. 2017, Sci, 358, 1556
Cowan, J. J., Sneden, C., Beers, T. C., et al. 2005, ApJ, 627, 238
Cowan, R. D. 1968, JOSA, 58, 808
Cowan, R. D. 1981, The theory of atomic structure and spectra (Berkeley, CA: Univ. California Press), doi:10.1525/9780520906150
Domoto, N., Tanaka, M., Wanajo, S., & Kawaguchi, K. 2021, ApJ, 913, 26
Eastman, R. G., & Pinto, P. A. 1993, ApJ, 412, 731
Eichler, D., Livio, M., Piran, T., & Schramm, D. N. 1989, Natur, 340, 126
Englemanr, R. J. 2003, JQSRT, 78, 1
Evans, P. A., Cenko, S. B., Kennea, J. A., et al. 2017, Sci, 358, 1565
Even, W., Korobkin, O., Fryer, C. L., et al. 2020, ApJ, 899, 24
Fontes, C. J., Fryer, C. L., Hungerford, A. L., Wollaeger, R. T., & Korobkin, O. 2020, MNRAS, 493, 4143
Freiburghaus, C., Rosswog, S., & Thielemann, F.-K. 1999, ApJL, 525, L121
Froese Fischer, C., Gaigalas, G., Jönsson, P., & Bieroń, J. 2019, CoPhC, 237, 184
Fujibayashi, S., Kiuchi, K., Wanajo, S., et al. 2022, arXiv:2205.05557
Fujibayashi, S., Wanajo, S., Kiuchi, K., et al. 2020, ApJ, 901, 122
Gaigalas, G., Zalandauskas, T., & Fritzsche, S. 2004, CoPhC, 157, 239
Gillanders, J. H., McCann, M., Sim, S. A., Smartt, S. J., & Ballance, C. P. 2021, MNRAS, 506, 3560
Gillanders, J. H., Smartt, S. J., Sim, S. A., Bauswein, A., & Goriely, S. 2022, MNRAS, 515, 631
Goriely, S., Bauswein, A., & Janka, H.-T. 2011, ApJL, 738, L32
Honda, S., Aoki, W., Ishimaru, Y., Wanajo, S., & Ryan, S. G. 2006, ApJ, 643, 1180
Hotokezaka, K., Tanaka, M., Kato, D., & Gaigalas, G. 2021, MNRAS, 506, 5863
Hotokezaka, K., Tanaka, M., Kato, D., & Gaigalas, G. 2022, MNRAS, 515, L89
Johansson, S., & Litzén, U. 1972, PhyS, 6, 139
Karp, A. H., Lasher, G., Chan, K. L., & Salpeter, E. E. 1977, ApJ, 214, 161
Kasen, D., Badnell, N. R., & Barnes, J. 2013, ApJ, 774, 25
Kasen, D., Metzger, B., Barnes, J., Quataert, E., & Ramirez-Ruiz, E. 2017, Natur, 551, 80
Kasliwal, M. M., Kasen, D., Lau, R. M., et al. 2022, MNRAS, 510, L7
Kawaguchi, K., Fujibayashi, S., Shibata, M., Tanaka, M., & Wanajo, S. 2021, ApJ, 913, 100
Kawaguchi, K., Shibata, M., & Tanaka, M. 2018, ApJL, 865, L21
Kawaguchi, K., Shibata, M., & Tanaka, M. 2020, ApJ, 889, 171
Kielkopf, J. F. 1971, AcSpe, 26, 371
Korobkin, O., Rosswog, S., Arcones, A., & Winteler, C. 2012, MNRAS, 426, 1940
Kramida, A., Ralchenko, Yu., Reader, J. & NIST ASD Team 2021, NIST Atomic Spectra Database v5.9, National Institute of Standards and Technology, Gaithersburg, MD, https://physics.nist.gov/asd
Kupka, F., Piskunov, N., Ryabchikova, T. A., Stempels, H. C., & Weiss, W. W. 1999, A&AS, 138, 119
Kurucz, R. L. 2018, in ASP Conf. Ser. 515, Workshop on Astrophysical Opacities (San Francisco, CA: ASP), 47
Lattimer, J. M., & Schramm, D. N. 1974, ApJL, 192, L145
Li, L.-X., & Paczyński, B. 1998, ApJL, 507, L59
Lucy, L. B. 2003, A&A, 403, 261
McCully, C., Hiramatsu, D., Howell, D. A., et al. 2017, ApJL, 848, L32
Metzger, B. D., Martínez-Pinedo, G., Darbha, S., et al. 2010, MNRAS, 406, 2650
Meyer, B. S. 1989, ApJ, 343, 254

Nicholl, M., Berger, E., Kasen, D., et al. 2017, ApJL, 848, L18
Perego, A., Radice, D., & Bernuzzi, S. 2017, ApJL, 850, L37
Perego, A., Vescovi, D., Fiore, A., et al. 2022, ApJ, 925, 22
Pian, E., D'Avanzo, P., Benetti, S., et al. 2017, Natur, 551, 67
Piskunov, N. E., Kupka, F., Ryabchikova, T. A., Weiss, W. W., & Jeffery, C. S. 1995, A&AS, 112, 525
Pognan, Q., Jerkstrand, A., & Grumer, J. 2022a, MNRAS, 513, 5174
Pognan, Q., Jerkstrand, A., & Grumer, J. 2022b, MNRAS, 510, 3806
Prantzos, N., Abia, C., Cristallo, S., Limongi, M., & Chieffi, A. 2020, MNRAS, 491, 1832
Roberts, L. F., Kasen, D., Lee, W. H., & Ramirez-Ruiz, E. 2011, ApJL, 736, L21
Roederer, I. U., Lawler, J. E., Sobeck, J. S., et al. 2012, ApJS, 203, 27
Rosswog, S., Sollerman, J., Feindt, U., et al. 2018, A&A, 615, A132
Ryabchikova, T., Piskunov, N., Kurucz, R. L., et al. 2015, PhyS, 90, 054005
Shibata, M., Fujibayashi, S., Hotokezaka, K., et al. 2017, PhRvD, 96, 123012
Silva, R. F., Sampaio, J. M., Amaro, P., et al. 2022, Atoms, 10, 18
Smartt, S. J., Chen, T.-W., Jerkstrand, A., et al. 2017, Natur, 551, 75
Sobolev, V. V. 1960, Moving envelopes of stars (Cambridge, MA: Harvard Univ. Press)
Tanaka, M., & Hotokezaka, K. 2013, ApJ, 775, 113
Tanaka, M., Hotokezaka, K., Kyutoku, K., et al. 2014, ApJ, 780, 31
Tanaka, M., Kato, D., Gaigalas, G., et al. 2018, ApJ, 852, 109
Tanaka, M., Kato, D., Gaigalas, G., & Kawaguchi, K. 2020, MNRAS, 496, 1369
Tanaka, M., Utsumi, Y., Mazzali, P. A., et al. 2017, PASJ, 69, 102
Utsumi, Y., Tanaka, M., Tominaga, N., et al. 2017, PASJ, 69, 101
Valenti, S., Sand, D. J., Yang, S., et al. 2017, ApJL, 848, L24
Villar, V. A., Cowperthwaite, P. S., Berger, E., et al. 2018, ApJL, 862, L11
Wanajo, S. 2018, ApJ, 868, 65
Wanajo, S., Sekiguchi, Y., Nishimura, N., et al. 2014, ApJL, 789, L39
Watson, D., Hansen, C. J., Selsing, J., et al. 2019, Natur, 574, 497